Universidad de Oviedo

Measurement of the WZ cross-section in proton-proton collisions with the CMS experiment at the LHC at CERN

Trabajo Fin de Máster

Autor:

Miguel Obeso Menéndez

Tutores:

Francisco Javier Cuevas Maestro

Santiago Folgueras Gómez

2022-2023

Contents

List of Figures

List of Tables

1 Introduction

With the discovery of the the W and Z bosons as two massive particles that intermediate the weak interaction, an answer was given to the possible merge between the electromagnetic and weak interactions, known as the electroweak theory. The study of particle physics in the electroweak sector continued to be carried out at increasing the center-of-mass energy until it was possible to achieve new processes. One of these processes was the production of two electroweak bosons W and Z simultaneously that has been measured using proton-proton collisions at the LHC by the CMS and ATLAS experiments, showing excellent agreement with the Standard Model predictions.

Now, with the start in 2022 of a new period of operation in the LHC at a new energy limit at a center-of mass of 13.6 TeV. The objective of this thesis is to provide a first measurement of the cross section of the diboson WZ process using the available data from the CMS experiment collected during the year 2022 at the center-of-mass energy of 13.6 TeV.

This document is organized as follows: An introduction to the Standard Model theory that describes particle physics, Sec. 2. Afterwards, there will be a description of the experimental device used (Sec. 3) and the reconstruction of events both experimentally (Sec. 4.1) and simulated according to the theory of the Standard Model (Sec. 4.2). Later we will describe the process that we are studying, its characteristics and how to proceed to carry out the measurement (Sec. 5). Finally, the results (Sec. 6) and the conclusions (Sec. 7) will be presented.

2 Standard Model

The Standard Model (SM) is known for being the most accurate theory capable of describing the physical reality of elementary particles and their interactions according to the Quantum Field Theory (QFT) which unifies our knowledge of the Special Relativity Theory and Quantum Mechanics. QFTs ared described by a Lagrangian, a scalar function able to describe a discrete system of particles with a finite number of degrees of freedom that allows us to extract equations of motion, conserved quantities, and other important results. Over the last century and nowadays, experiments have been designed with the goal of on providing new knowledge that can help probe the veracity of this model.

The discover of Higgs boson in 2012 has generated the beginning of new unexplored horizons of particle physics that the SM theory can not explain. These are englobed as physics beyond the Standard Model (BSM) with conjectures such as: the possible union of the quantum physics and gravity, the meaning of the Higgs boson mass, the search for dark matter candidates, the existence of neutrinos masses and others.

The Standard Model is composed by three fundamental interactions: strong (S), weak (W) and Electromagnetic (EM). The latter two can be merged in a single interaction known as electroweak interaction (EW). In order to have a compatible model with the Special Relativity, the universe is defined as a Minkowski-like spacetime, a combination of three-dimensional Euclidean space with time in a four-dimensional manifold, whose lagrangian is invariant under gauge transformations. Such theories have the characteristic of being invariant under local transformations of the $SU(x)$. These are called *Local Gauge Symmetries*, which are special unitary groups of different dimensions depending of the interaction. The strong interaction is described by a $SU(3)$ group. Also, to describe the electroweak interaction, we use two different groups: the

$SU_L(2)$ to describe the proper interaction and the $U_{\Upsilon}(1)$ for the study of the weak isospin and hypercharge.

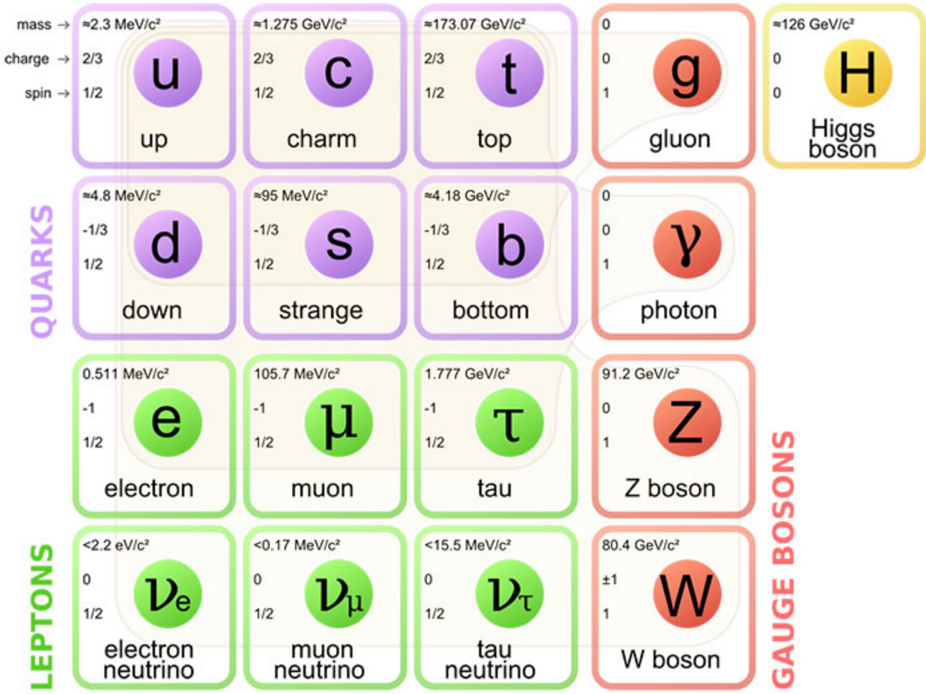

Figure 1: Clasification of all the particles described by the Standard Model according to their properties (spin, charge and mass), [45].

The Lagrangian of the Standard Model is composed of different terms associated with the presence of fields and interactions that these generate on matter. As a whole it describes the existence of 17 particles and their possible interactions between them. All the fundamental particles that make up the Standard Model are included in Fig. 1. In it can be distinguish between twelve fermions, developed in Sec. 2.1. The intermediate particles of the interactions are what we call bosons, Sec. 2.2. Make a special mention of the Higgs boson, the basis of the Higgs mechanism that will be explained in Sec. 2.3.

The characteristics of elementary particles determine their interaction with the fundamental forces of our universe. Electrically charged particles will experience the electromagnetic force. On the other hand, those that have another property called *color charge*, will undergo the strong interaction. In addition, the weak interaction is not defined by any quantity, however, it is closely (but not trivially) related to characteristics such as: mass, particle stability or half-life.

2.1 Fermions

The fermions are the twelve elementary particles of the Standard Model with spin $s = 1/2$. Depending on which of the fundamental interaction they suffer, we can divide them between six leptons and six quarks. The leptons are the fundamental particles which have no colour charge, so they only suffer the electroweak interaction and don't suffer the strong interaction. The charged leptons with $q_e = -1$[1] are electrons (e), muons (μ) and taus (τ) and the neutral leptons ($q_e = 0$) that are the neutrinos: ν_e, ν_μ and ν_τ. On the other hand, the quarks have colour and electromagnetic charge, so they can be affected by both interactions, electroweak and strong. Also quarks are classified in association with the electromagnetic charge: up-like quarks: u, c and t which have $q_e = 2/3$ and the down-like: d, s and b with $q_e = -1/3$. The QFT that describes the behaviour of fermions, uses a spinor representation of Lorentz Group. The kinetic component of the lagrangian [2]:

$$\mathcal{L}_{Dirac} = \bar{\Psi}\gamma^\mu \partial_\mu \Psi \tag{1}$$

where the γ^μ are the representation of the Pauli matrices in the Clifford algebra ($Cl_{1,3}$, [36]) that build certain anti-commutation rules and the functions (Ψ, $\bar{\Psi}$) that represent the field of a fermionic particles and the Dirac adjoint of the field

[1] normalized with the charge of the electron in absolute value that correspond to $e = 1.602 \cdot 10^{-19}\ C$.

[2] See more in: [30], [42] or [32].

($\bar{\Psi} = \Psi^{\dagger}\gamma^0$).

$$\Psi_L = \frac{1-\gamma^5}{2}\Psi \tag{2}$$

$$\Psi_R = \frac{1+\gamma^5}{2}\Psi \tag{3}$$

where $\gamma^5 = i\gamma^0\gamma^1\gamma^2\gamma^3$. It allow us to assume the presence of a mass term on the lagrangian, that could be implemented like:

$$\mathcal{L}_{Dirac}^{mass} = -m(\bar{\Psi}_L\Psi_R + \Psi_L\bar{\Psi}_R) \tag{4}$$

2.2 Vector bosons

The $SU_L(2)$ group define three fields denoted as W_μ^i where $i = 0, 1, 2$ and are associated with vector bosons of spin $s = 1$. The lagrangian for a massless free fields is defined:

$$\mathcal{L}_W = -\frac{1}{4}W_{\mu\nu}^i W_i^{\mu\nu} \tag{5}$$

$$W_{\mu\nu}^i = \partial_\mu W_\nu^i - \partial_\nu W_\mu^i + g\varepsilon_{ijk}W_\mu^j W_\nu^k \tag{6}$$

If one proceeds to consider that the associated particles could have mass, it is found that the fields cannot have an explicit mass term due to the rules of transformation of the gauge group $SU(2)$. In other words, it is not invariant under a Local Gauge Transformation. The mass of boson particles will be discussed later in Sec.2.3.

On the other hand, the gauge group U(1) has associated a vector field B with a Lagrangian similar to that represented for SU(2) in the Eq.5.

$$\mathcal{L}_B = -\frac{1}{4}B_{\mu\nu}B^{\mu\nu} \tag{7}$$

$$B_{\mu\nu} = \partial_\mu B_\nu - \partial_\nu B_\mu \tag{8}$$

Analogous to the previous group, the theory does not allow a mass term in this field. In addition, studying the conserved quantity of the system known as hypercharge, allows us to study the charge associated with fermions that is consistent with that shown in the previous section. Finally, the electroweak interaction can be described by a single total Lagrangian that takes into account bosons and possible interactions with fermions.

$$\mathcal{L}_{EWK} = -\frac{1}{4}B_{\mu\nu}B^{\mu\nu} - \frac{1}{4}W^{i}_{\mu\nu}W^{\mu\nu}_{i} + \bar{e}_R\gamma^{\mu}D^{e_R}_{\mu}e_R + \bar{u_R}\gamma^{\mu}D^{u_R}_{\mu}u_R + \\ + \bar{d_R}\gamma^{\mu}D^{d_R}_{\mu}d_R + \bar{q_R}\gamma^{\mu}D^{q_L}_{\mu}q_L + \bar{l}_L D^{l_L}_{\mu}l_L \tag{9}$$

where D^X_μ represents the covariant derivative and is define in terms of weak isospin, hypercharge and the original partial derivative.

$$D^X_\mu = \partial_\mu - igI^X_3\sigma_i W^i_\mu - ig\prime\Upsilon B_\mu \tag{10}$$

The Eq.9 shows that a theory of fermions interacting through the SU(2) gauge field exists only if the fermions are massless.

2.3 Electroweak symmetry breaking

Although SM theory predicts that fermions and bosons are massless, the experimental evidence obtained shows that both, bosons and fermions have the property of non-zero mass. That is why it was necessary to define a mechanism that would make this possible. The Higgs-Brout-Englert mechanism [38], [31] which proposes the addition of a scalar field in the Lagrangian that explains how these particles acquire mass by interaction with the new proposed field. It allows to relate the vector bosons explained from the Standard Model theory with those observed in the reality: $W^{\pm}$, Z and γ. Defining a complex scalar field such as:

$$\mathcal{L}_\phi = D_\mu\phi D^\mu\phi - \mu^2\phi^\dagger\phi + \frac{\lambda}{2}(\phi^\dagger\phi)^2 \tag{11}$$

where μ and λ are free parameters of the model. The general expression of the scalar field, Eq. 11, must be modified for implementation in 9 and explain the presence of mass that is measured experimentally. For this, the lagrangian term of the scalar field is described with a both triple and quadruple self-coupling interactions. The associated particle to this field is the called the Higgs boson:

$$\mathcal{L}_H = D_\mu H D^\mu H - \frac{\mu^2}{2} H^2 + \sqrt{2}\mu H^3 + \frac{\lambda}{2} H^4 + \mathcal{O}(vH) + \mathcal{O}(v^2) \tag{12}$$

where the covariant derivatives shows the coupling with the gauge bosons and at least three fields are needed and the last term is in association with the presence of mass in this bosons. This last element of the lagrangian that are independent of the Higgs, could be extended like in the next expression:

$$\mathcal{L}_{H_{indep}} = \frac{v^2}{2}(W_\mu^1,\, W_\mu^2,\, W_\mu^3,\, B_\mu) \begin{pmatrix} \frac{-g^2}{4} & 0 & 0 & 0 \\ 0 & \frac{-g^2}{4} & 0 & 0 \\ 0 & 0 & \frac{-g^2}{4} & \frac{-gg\prime}{4} \\ 0 & 0 & \frac{-gg\prime}{4} & \frac{-g^2}{4} \end{pmatrix} \begin{pmatrix} W_\mu^1 \\ W_\mu^2 \\ W_\mu^3 \\ B_\mu \end{pmatrix} \tag{13}$$

This couplings generate the mass terms for the W_μ bosons. The matrix is diagonalizable and a total of four different eigenvalues of the mass can be obtained. Diagonalizing the upper part, it is possible to get the first two massive bosons:

$$W_\mu^+ = \frac{1}{\sqrt{2}}\left(W_\mu^1 + iW_\mu^2\right) \tag{14}$$

$$W_\mu^- = \frac{1}{\sqrt{2}}\left(W_\mu^1 - iW_\mu^2\right) \tag{15}$$

which represents the charged W boson of opposite sign with a mass term $m_W = \frac{gv}{2}$. In the other hand, diagonalizing the lower part of the matrix, it can be found others two different mass eigenstates:

$$Z_\mu^0 = \frac{1}{\sqrt{g^2 + g\prime^2}}\left(gW_\mu^3 + g\prime B_\mu\right) \tag{16}$$

$$A_\mu^0 = \frac{1}{\sqrt{g^2 + g\prime^2}}\left(g\prime W_\mu^3 + gB_\mu\right) \tag{17}$$

where they represent the no charged Z boson with mass $m_Z = \frac{v}{2}\sqrt{g^2 g\prime^2}$ and the neutral and massless electroweak boson, called photon (γ).

The Standard Model does not define a value for the Higgs boson mass and the μ, λ parameters of the mechanism, which must be determined from experimental results. The mass of the gauge bosons and the strengths of the electroweak interactions are highly dependent and linked to each other. These can be related through a Standard Model parameter called Weinberg angle or weak mixing angle (θ_w):

$$\frac{m_W}{m_Z} = \frac{g}{\sqrt{g^2 + g\prime^2}} = cos(\theta_w) \tag{18}$$

which is of great relevance for experimental studies of the bosons mass properties and their couplings.

2.4 Yukawa coupling

Previously, it was said that the theory of fermions interacting through the $SU(2)$ group exists only if the fermions have no mass. With the possible interaction of these with the Higgs mechanism, it is possible to explain the presence of mass in fermions as experimentally observed.

$$\mathcal{L}_{Yukawa} = -y_l \bar{l}_L \phi e_R - y_d \bar{q}_L \phi d_R - y_u \bar{q}_L \varepsilon \phi^\dagger u_R \tag{19}$$

where the terms y_X are free parameters of the model called Yukawa couplings. Specifying the system with the mass and parameter values associated with the Higgs boson, we obtain:

$$\mathcal{L}_{Yukawa} = \frac{y_l v}{\sqrt{2}} \bar{e}_L e_R - \frac{y_d v}{\sqrt{2}} \bar{d}_L d_R - \frac{y_u v}{\sqrt{2}} \bar{u}_L u_R + \mathcal{O}(Hff) \tag{20}$$

where the associated mass for all the charged leptons and quarks are $m_f = \frac{y_f v}{\sqrt{2}}$ and the uncharged leptons (neutrinos) still massless. According new generations of fermions called flavours are include in the Standard Model, the definition of the

Yukawa coupling and fermions mass become more difficult to estimate.

The connection between the electroweak interaction from different families of quarks, are determinate by the Cabibbo-Kobayashi-Maskawa matrix (CKM-matrix) which encodes the coupling of the $W^{\pm}$ bosons to a pair of quarks.

$$V_{CKM} = \begin{pmatrix} V_{ud} & V_{us} & V_{ub} \\ V_{cd} & V_{cs} & V_{cb} \\ V_{td} & V_{ts} & V_{tb} \end{pmatrix} \tag{21}$$

2.5 Boson polarization

Analogous to photon polarization in classical physics, it also occurs in Quantum Field Theory. When dealing with massless bosons such as the photon, the longitudinal polarization is parallel to the momentum of the particle so they can not interact. On the other hand, the massive bosons shows longitudinally-polarized modes as a consequence of the scalar field mechanism, where the vector boson absorbs an additional polarization degree of freedom.

Different observations made in the production of the vector bosons W and Z, show polarized final states even when the particles of the collision did not show polarization. For different polarization fractions: left polarization (f_L), right polarization (f_R) and the longitudinally-polarized state (f_0). Redefining the Weinberg angle, its possible to create a relation between the polarization an the differential cross section for W and Z bosons:

$$\frac{d\sigma}{\sigma d\, cos\, \theta^{W\pm}} = \frac{3}{8}\left[(1 \mp cos(\theta^{W\pm}))^2 f_L^W + (1 \pm cos(\theta^{W\pm}))^2 f_R^Z + 2sin^2(\theta^{W\pm}))f_0^W\right] \tag{22}$$

$$\frac{d\sigma}{\sigma d\, cos\, \theta^{Z}} = \frac{3}{8}\left[(1 + cos^2(\theta^{Z}) + 2c\, cos(\theta^{Z}))f_L^Z + (1 + cos^2(\theta^{Z}) - 2c\, cos(\theta^{Z}))f_R^Z + 2sin^2(\theta^{Z})f_0^Z\right] \tag{23}$$

where σ is the production cross section of a generic process which involves any vector boson depends of the massive boson polarization.

2.6 Beyond Standard Model physics

The Standard Model is not able to explain everything in the particle physics. There is a lot of things that do not have an explanation and is needed to be explain with alternative theories that build upon the SM to complement the model. These are the Beyond Standard Model theories which includes dark matter, neutrinos physics, supersymmetry and others.

2.7 Diboson production

The massive boson pairs production are processes in which the final state is coming from a gauge diboson state like WW, WZ and ZZ. This kind of processes are really important for the study of the electroweak sector, Higgs understanding and the search for new physics.

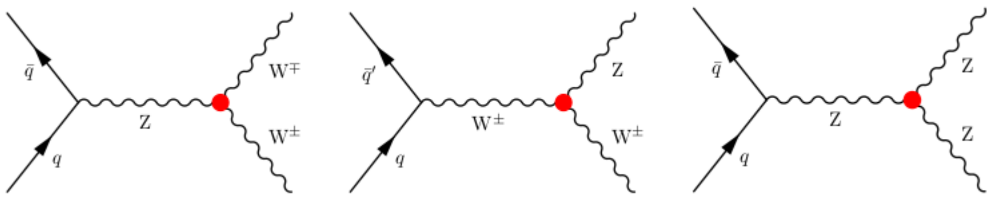

Figure 2: Triple gauge coupling processes of ordered vector bosons in production of WW, WZ and ZZ.

Massive diboson production channels can produce triply coupling processes. This type of processes gives access to a precision study on the physics of massive vector bosons and on the theory of the Standard Model in the electroweak sector. These type of diagrams can be seen at leading order (LO)[3] in QCD and next to leading order (NLO) in Fig. 13, and will be explain in Sec. 5.2. These processes are closely related to the non-Abelian structure of the electroweak sector of Eq. 5 and Eq. 6. In addition, the Eq. 18, relates the masses of the W and Z bosons to the strength of a triple coupling.

[3] LO and NLO refer to the first and second order terms of the production contributions of a given process in perturbation theory.

3 Experimental device

3.1 LHC particle accelerator

The Large Hadron Collider (LHC) is a particle accelerator located at the CERN (European Organization for Nuclear Research) complex in Geneva, Switzerland. It is known for being the biggest and most powerful accelerator ever made. The LHC is a circular accelerator with a longitude of 27 km, built under the ground. The goal of this accelerator is to study high energy physics (HEP) in order to measure the properties of particles and have a more precise understanding of the Standard Model parameters.

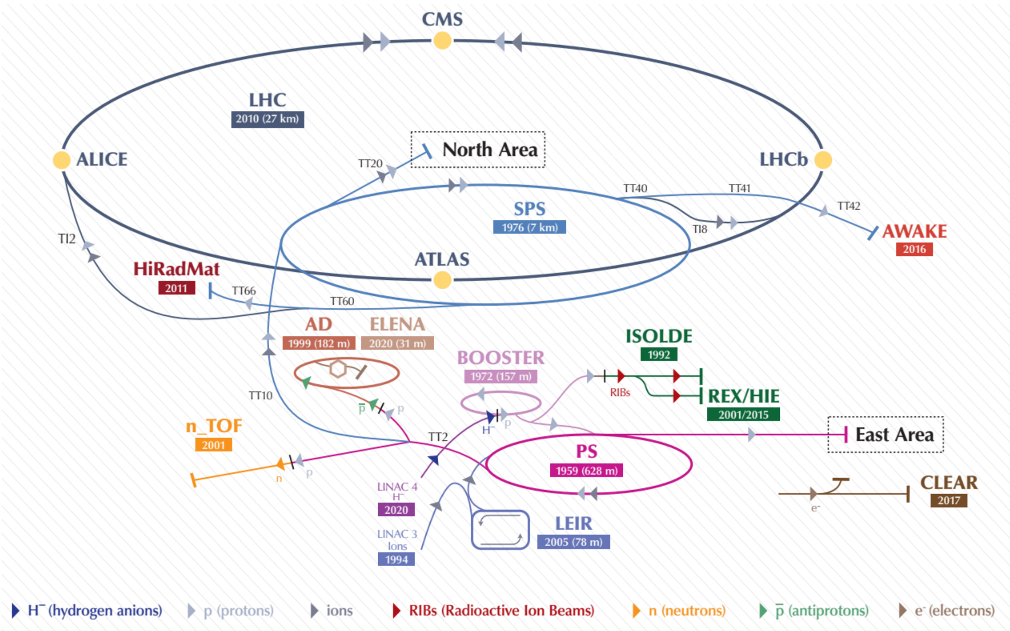

Figure 3: Schematic representation of CERN accelerators and their detectors [34].

This accelerator was planned and built between 1998 and 2008. It has been operating since 2010 until today at different energies and data taking periods usually referred to as *Runs*. The first (Run 1) was during the year 2010 at a center-of-mass energy of $\sqrt{s} = 7$ TeV until 2013. The second (Run 2) was longer-lasting, from 2016 to 2018 with an energy of $\sqrt{s} = 13$ TeV. As of July 5th 2022, the LHC started the so-called Run 3 at a brand new energy regime of $\sqrt{s} = 13.6$ TeV that this implies an energy of 6.8 TeV in each beam before the collision.

LHC collides protons, so different variables must be taken into consideration as will be discussed later. These collisions take place at different points of the accelerator where detectors are located to collect data and information about the events. In the LHC, there are a total of four detectors: CMS, ATLAS, LHCb and ALICE. CMS and ATLAS are general purposes detectors for the study of different high-energy physics processes. On the other hand, ALICE is dedicated to the study of heavy ions, and LHCb's study focuses on the analysis of the b quark.

The LHC has been designed to accelerate protons in a chain of circular accelerators, see Fig. 3. The direction followed by the particles is controlled by a set of superconducting dipole magnets capable of creating a magnetic field of 8.33 T placed along the circumference of the LHC. The function of accelerating the particle bunches is also due to the presence of eight radiofrequency cavities at a temperature of $T = 4.5$ K that induce an oscillating electric field with a frequency of $\nu = 400$ MHz. Additionally, there is a compression of the bunches in order to reduce their area and increase the collision probability using quadrupole and hexapole magnets.

3.1.1 Luminosity at the LHC

The protons that travel through the LHC move in bunches containing around 10^{11} particles. The distance between these bunches and their number has been optimized in order to obtain the highest possible number of collisions to be studied and stored.

Therefore, it is interesting to know the overall number of collisions that occur. Particle beams travel at speeds close to the speed of light in a ring of a given length (l), where the bunches have an ellipsoidal shape assumed to be a Gaussian distribution that can describe the collision surface using two parameters: $\Sigma = 4\pi\sigma_x\sigma_y$. If each particle beam consists of a fixed and controlled number of bunches (n_b), and each bunch has a number of particles N_1 and N_2 in each beam respectively, it is possible to define a quantity that allows us to compute the number of particles traveling through the accelerator; this quantity is known in particle physics as instantaneous luminosity which allows to measure the number of particles that are likely to undergo a collision per unit area and time:

$$\mathcal{L} = n_b \frac{N_1 N_2}{\Sigma} f_{coll} = n_b \frac{N_1 N_2}{4\pi\sigma_x\sigma_y} \frac{l}{c} \tag{24}$$

which is in units of $\mathrm{cm}^{-2}\mathrm{s}^{-1}$. Generally, in particle physics, it is of interest to study this quantity over a certain time interval. This magnitude is called integrated luminosity and is calculated as:

$$L = \int \mathcal{L}\, dt \tag{25}$$

It is usually expressed in units of barns (with equivalence of $1\,\mathrm{barn} = 10^{-28}\mathrm{m}^2$). The recorded data so far from Run 3 in the CMS detector at the LHC is a total of $40.52\,\mathrm{fb}^{-1}$ from the delivered luminosity of the accelerator, which was $44.23\,\mathrm{fb}^{-1}$ as shown in Fig. 4.

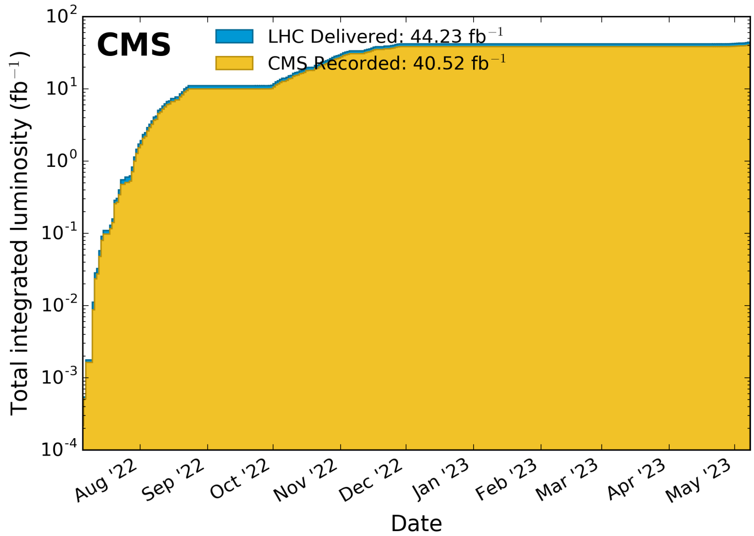

Figure 4: Cumulative delivered and recorded luminosity versus time during 2022 and 2023 [12].

In addition to this, another important duty is to recognize that these particles come from the main collision, which represents the more energetic collisions found in a event. In the LHC, with an instantaneous luminosity of $\mathcal{L} \approx 2 \cdot 10^{34}\,\mathrm{cm}^{-2}\mathrm{s}^{-1}$, a separation between the bunches collisions $\nu \approx 40\,\mathrm{MHz}$, an inelastic cross section for protons in the bunches of $\sigma_{inel}^{pp} = 80.0\,\mathrm{mb}$ at an energy of $\sqrt{s} = 13.6\,\mathrm{TeV}$, it is expected that for each event would be around $N \approx 40$ simultaneous collisions with different interaction vertices as is observed in Fig.5.

The goal of identifying all pileup collisions formed in each event is one of the most difficult challenges to study in any hadron collisions. That is why it is necessary to carry out a highly precise study to end up with a single collision vertex that we call the *primary vertex*.

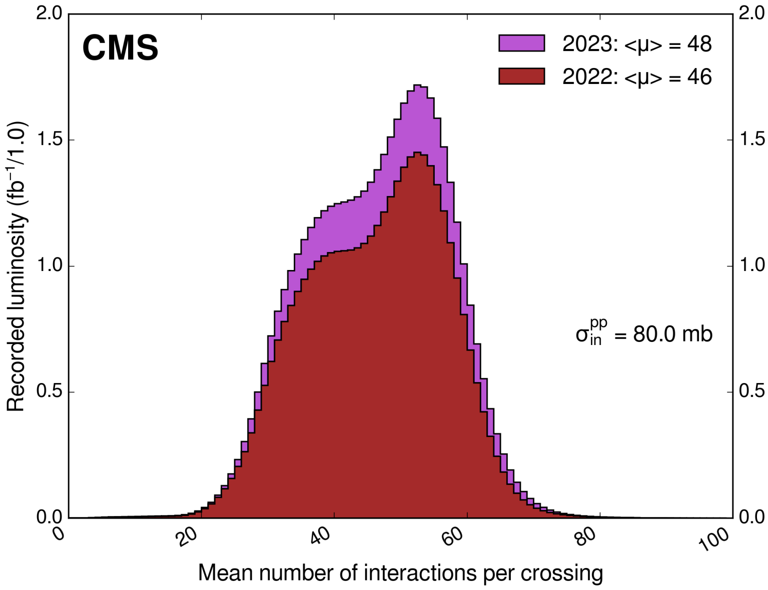

Figure 5: Distribution of the average number of interactions per crossing (pileup) for pp collisions in 2022 (red) and 2023 (light purple). The overall mean values and the minimum bias cross sections are shown, [14].

3.1.2 Cross section in hadron physics, QCD, and partons

The production cross-section is a crucial quantity in particle physics that can be related to the probability of a specific production process occurring during the study of experimental particle collisions. This probability depends on two fundamental variables: the collision energy and the type of particle undergoing the interaction.

In recent years, hadrons are being used as the collision tool for experiments related with the particle physics. These are not elementary particles, but are compose of different states of quarks and gluons linked by the strong interaction described by quantum chromodynamics (QCD).

The particles that compose a hadron are called *partons*. In the LHC, it is used proton as a source of collisions. The cross section of a certain process in which two components (a and b) interact, obtaining a final state (X) such that $a + b \to X$, is described by:

$$\sigma_X = \sum_{a,b} \int_0^1 dx_i dx_j f(x_i) f(x_j) \hat{\sigma}(ab \to X) \tag{26}$$

where $\hat{\sigma}$ represents the probability with which a parton of each colliding hadron will interact, $x_i = \frac{\vec{p_i}}{\vec{p}_{proton}}$ characterizes the ratio of the parton's momentum respect to the total from the hadron. A Parton Distribution Function (PDF), showed as $f(x_i)$, is an object that describes the probability to find a parton of the given flavour and momenta. The value and ratio of this functions for different flavours depends on the energy. This is shown in Fig. 6. In the collisions carried out at the LHC with energies that reach 13.6 TeV, we can see by observing the previous Fig. 6, that they will be mostly gluon-gluon collisions.

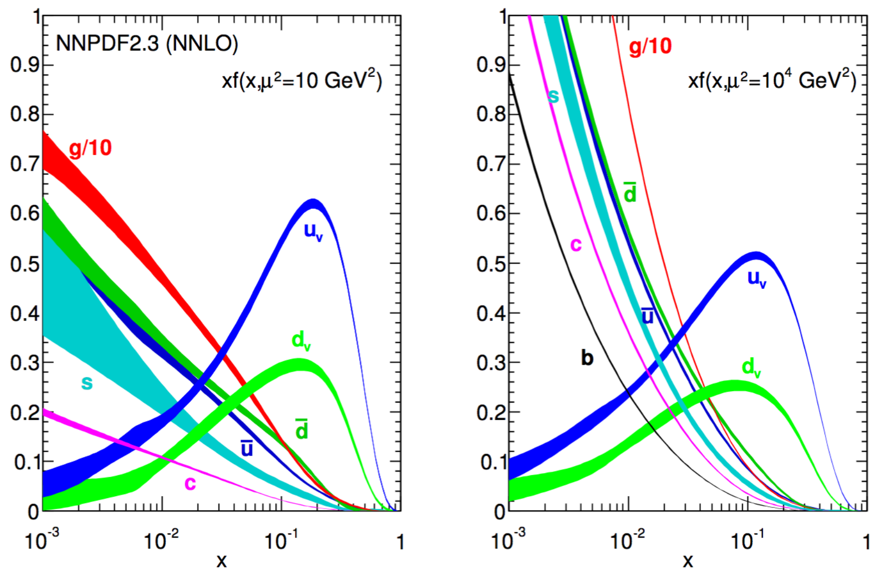

Figure 6: Parton distribution functions generated at next-next-to-leading order (NNLO) in QCD proton study at an scale $10\,GeV$ and $10^4\,GeV$ with the confidence level, [39].

3.2 CMS detector

The Compact Muon Solenoid (CMS) is a cylindrical detector installed at the LHC with dimensions of 21.6 in length, 14.6 m in diameter and weighing $14 \cdot 10^3$ tons. It is possible to divide the detector in two main sections. The first is the so-called *barrel*, located around the cylinder and covers almost the entire detector surrounding a superconducting solenoid. The second part is *the endcap* that is in the bases of the cylinder being the part corresponding to the orthogonal plane to the direction of the collision.

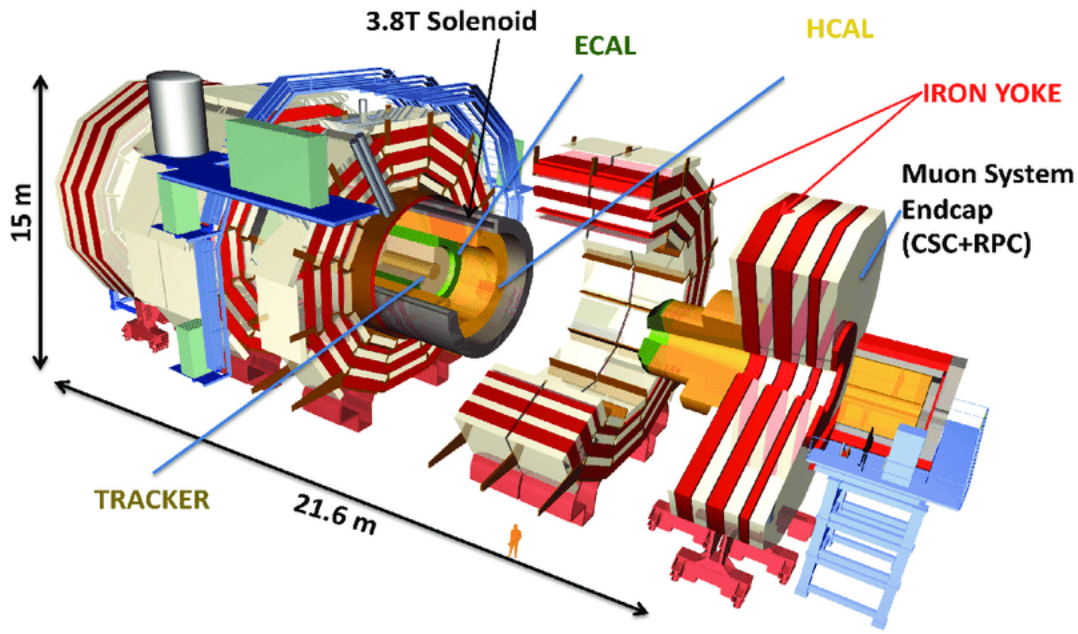

Figure 7: Schematic view of the CMS detector compared to the size of a person where the dimensions and the different sub-detectors are indicated [35].

The CMS is composed of four sub-detectors, each with a certain technology, function and responsible for the detection and identification of different particles. These are the tracker, electromagnetic calorimeter (ECAL), hadronic calorimeter (HCAL) and muon system. Also, there is a solenoid magnet that lies between the hadronic calorimeter and the muon system and which is known for being the largest superconducting solenoid ever built and reaches a magnetic field of 3.8 T. All these components can be identify in Fig.7 and will be described in detail later.

The choice of a compact design for CMS aims to maximise detector geometrical acceptance, which is defined as the geometrical region in which particles can be identified. This allows for CMS to reach great efficiencies in particle identification.

3.3 Coordinates system

For the study of the interactions that take place in the CMS detector, the origin is defined as the nominal positions where the collisions take place. Observed from the point of view of a Cartesian system and orthogonal axes, the z-axis is defined in the direction in which the proton beam circulate. The normal plane to this axis is formed by the x, y-axes. But, due to the structure of the detector, a non-Euclidean coordinates are used to describe the trajectories of the particles formed in the interaction. The usual spherical coordinates (r, θ, ϕ) are not convenient to measure the properties of the particles, so they are re-defined as: $r \to p_T$, $\theta \to \eta$ and the azimuth angle (ϕ) does not change. The p_T is the four-momentum in the transverse plane (XY) of the particle and η is just a Lorentz invariant transformation of the polar angle called *pseudorapidity*.

$$p_T = \sqrt{p_X^2 + p_Y^2} \tag{27}$$

$$\eta = -ln\left[tan\left(\frac{\theta}{2}\right)\right] \tag{28}$$

$$\phi = arctg\left(\frac{y}{x}\right) \tag{29}$$

It is also possible to define a variable that measures the angular distance between two particles in terms of these angles such that: $\Delta R = \sqrt{(\eta_1 - \eta_2)^2 + (\phi_1 - \phi_2)^2}$. The limit between the barrel and the endcap can be set around at $\eta \approx 1$, where the domain of this coordinate system angles are $\eta \in [0, \infty)$ and $\phi \in [0, \pi]$. According with the CMS geometry it is $\eta \in [0,\, 3]$ and $\phi \in [0, \pi]$.

3.4 CMS sub-detectors

3.4.1 The silicon tracker

The tracker is the innermost sub-detector of the CMS. It is the responsible to get a precise reconstruction of the charged particles trajectories (*tracks*). The tracker is made up of $66 \cdot 10^6$ small silicon pixels with a very high granularity which provides a transversal precision of $10\,\mu m$ and a longitudinal one of $20\,\mu m$. This works by receiving and measuring an energy signal received from the emitted electrons due to the ionization of silicon atoms after charged particles pass close to them. The tracker covers a section of $|\eta| \in [0,\, 2.4]$. The high number of pixels and sensors makes the system have a high granularity and sensitive to the identification of pile-ups and the main collision. For more information: [20].

3.4.2 Electromagnetic calorimeter

After the tracker, the second sub-detector is the electromagnetic calorimeter. It is designed to absorb the majority of electromagnetically interacting particles that travels through it such as photons or electrons. In the CMS detector, the ECAL is a solid scintillator composed with high density crystals of lead tungsten oxide ($PbWO_4$). This material have a greatly radiation resistance making it ideal for an ECAL situated relatively close to the collisions, thus avoiding possible residual radiation.

It is made up of $7 \cdot 10^3$ crystals in the endcap and $6.12 \cdot 10^4$ in the barrel. There is also another element installed in the ECAL-endcap, called *preshower*. This is composed of silicon and lead and validates the detection and differentiation of some particles with a significant kinetic component in the z axis. For example, to identify the decay mode of a neutral pion ($\pi^0 \rightarrow \gamma\gamma$). More information about preshowers could be found in [46]. The large number of crystals allows the calorimeter to have a great precision measuring the energy of this particles.

The electromagnetic calorimeter covers a section of $1.4 < |\eta| < 3.0$ and a distance of 4 m in the endcap and $|\eta| < 1.4$ and 160 cm in the barrel. For more information: [21].

3.4.3 Hadronic calorimeter

As the ECAL, the hadronic calorimeter is the responsible to absorb the energy of hadrons or particles made with quarks or gluons. It occupied a region of $|\eta| < 1.3$ and a distance of 2.8 m in the barrel, and $1.3 < |\eta| < 5.0$ with a distance of 15.6 m in the endcaps. This two parts are made up of alternated brass layers which absorbs and detects the energy. Also, in this sub-detector, a new region has been include covering the possibility of detecting hadrons with higher values of the pseudorapidity, with $3.0 < |\eta| < 5.0$ and 11.2 m in the Z axis. This part is composed by steel layers that is more resistant for radiation. For more information: [22].

After the HCAL, there is a last scintillator to absorb the possible residual hadronic radiation before the muon chamber.

3.4.4 Muon system

The muons are particles that have a good penetrative capacity. They pass through all the CMS sub-detectors, leaving only a few hits on the tracker and depositing only a small amount of energy in the calorimeters. The muon system is able to identify muons with an extraordinary efficiency.

The muon system covers a detection plane of $25 \cdot 10^3$ cm^2 is a system made up of three different types of technologies: Drift Tubes (DT), Cathode Strip Chamber (CSC), Resistive Plate Chamber (RPC). This entire system of muon chambers is integrated into 4 different layers within a large iron structure called iron yoke whose function is to limit the magnetic field (Sec. 3.5) and stop all remaining particles. The only ones that are not stopped by this structure are muons and neutrinos.

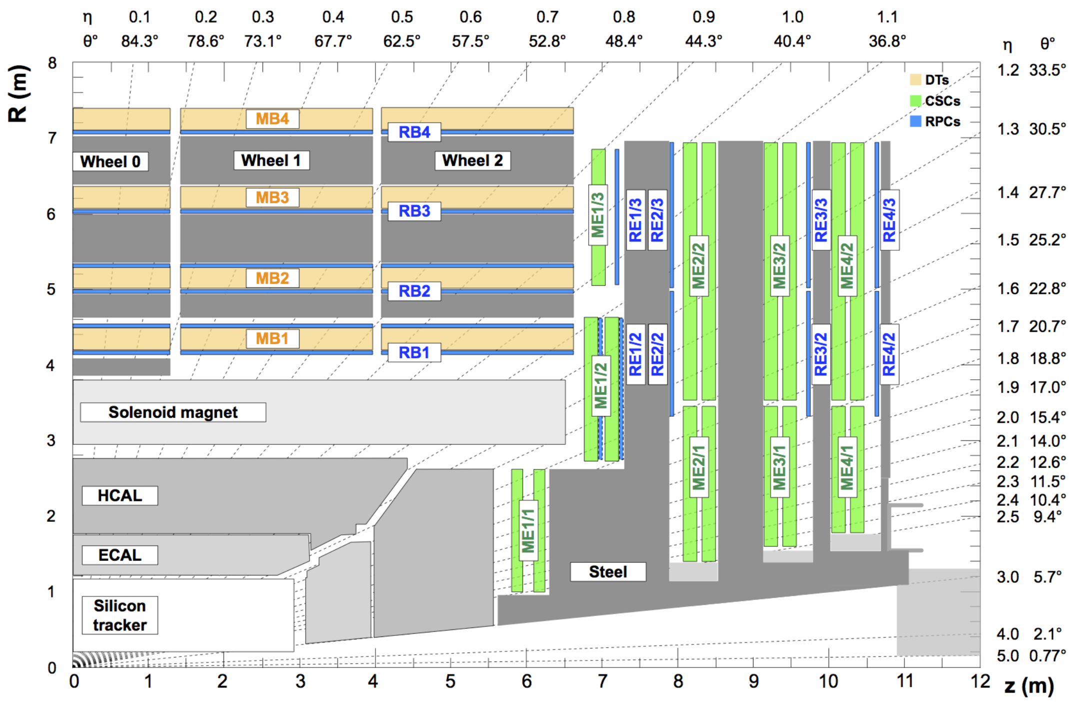

Figure 8: Representation of a section of the CMS muon detector where the different chambers can be differentiated according to the colors, [43].

The Drift Tubes are located on the detector barrel. These are focused on tracking muons with very high momentum for their identification and reconstruction. The DTs are usually associated with central pseudorapidity values.

The CSC chambers were chosen to be located in the endcaps due to their efficiency in areas where the magnetic field is not uniform, covering a pseudorapidity of $0.9 <$

$\eta < 2.4$.

Finally, the resistive plate chambers are gaseous parallel-plate detectors that are used in both: barrel and endcap, as a complementary sub-detector. The RPC have a high detection efficiency and works faster than the others chambers. The presence of a gas in its interior causes that after a muon go across the chamber, ionized electrons are emitted in a cascade. These can be distinguished in the Fig. 8 in blue color. For more information: [23].

3.5 The solenoid magnet

One of the most representative parts of the CMS is an iron solenoid magnet situated between the hadronic calorimeter and the muon chambers. This manages to create a nominal magnetic field of $B = 4.2$ T with the idea of using the Lorentz forces ($\vec{F} = q(\vec{E} + \vec{v} \times \vec{B})$) to bend the trajectory of the particles and through the curvature obtain the momentum of the particles.

3.6 The trigger system

According to what we explained in Sec. 3.1.1, in the CMS experiment, bunches of 10^{11} protons collide every $\Delta t = 25$ ns , which is the delay between two different bunches. This means that collisions occur with a frequency of 40 MHz. Large amounts of data are produced every second for which there is not enough physical storage for them.

Therefore, a quick selection of those events with relevant information for the study of physics is made. This useful tool to reduce the amount of data that is going to be stored and discard those processes that are of no interest, is called a trigger.

The trigger designed in CMS has two different levels. The first, called Level 1 Trigger (L1T) is hardware-based and reduce the information to 100 kHz. The second, High Level Trigger (HLT), is based on a software system. This is capable of storing information with a frequency of 1 kHz with criteria such as:

- The detection of specific particles of interest.
- High energy absorbed in the calorimeters.
- Some kinetic requirements of the particles (momentum, pseudorapidity,...).

First of all, the L1T studies the information provided by the calorimeters and the muon system. Using an algorithm, the trigger reduce the generated information to around 1/400. The events selected as favorable by the L1T are sent to the HLT. This trigger makes a more strict selection using all the information provided by all the sub-detectors. The HLT use an algorithm to make a basic object reconstruction. The accepted events are stored to be reconstructed and analyzed.

4 Event reconstruction and simulation

The events from the CMS experiment that pass the trigger selection criteria, explained in Sec. 3.6, are stored as what is called *raw data*. Once safely stored, so that this data is not lost, a less urgent process begins. This process consist in a more detailed and careful reconstruction of the particles that participate in the event to provide a complete description of the kinematic properties of the particles produced in the collision and other subsequent evolution processes.

4.1 Event reconstruction

For the reconstruction of different events in charge of identifying candidates for physical objects using the information provided by the sub-detectors, is used an algorithm called *Particle Flow* (PF). The algorithm is based on the kinematic and geometric reconstruction of the event to finally relate this physical objects with particles such as: photons, electrons, charged hadrons, neutral hadrons or muons. For more detailed information on the PF algorithm, see [13].

First, the tracks of charged particles that have been deposited in the tracker (Sec. 3.4.1) are studied. For this, an iterative algorithm is used that reconstructs the trajectory of a particle for each iteration, eliminating the previously reconstructed whats makes it easier and allows for less strict identification criteria as the algorithm advances. After the identification of the hits of charged particles, the vertices of the interactions are reconstructed. The vertex with the highest quadratic sum of momentum, will be considered the *main vertex*. The rest are interactions that we associate with the pile-up.

After this, the next step is to observe the tracks in the muon chambers and finally to examine the energy deposited in the two calorimeters (ECAL and HCAL). Next, it will be explained how the different particles are identified. In addition, the Fig 9 outlines the energy depositions of the different particles in the sub-detectors.

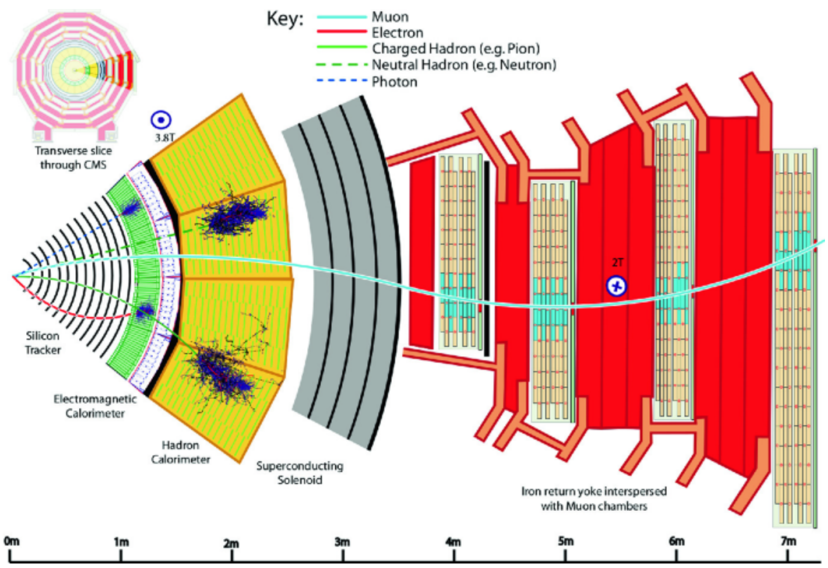

Figure 9: Representation of the trajectories obtained from each type of particle that are observed, measured and reconstructed in the CMS detector and the different interactions with the sub-detectors, [28].

4.1.1 Muon reconstruction

These are reconstructed from the signals deposited in the tracker (Sec. 3.4.1) and in the muon chambers (Sec. 3.4.4). According to what information is used to identify and reconstruct them, there are three types of muons:

- **Standalone muons:** Use only the depositions in the muon chambers (DT, CSC, RPC).
- **Tracker muons:** Reconstructed from the tracker but matching with the depositions located in the muon chambers.

- **Global muons:** Standalones muons candidate whose track is matched to another in the tracker, but in this cases, it is made a global fit to recalculate the trajectories using the both sub-detectors information.

To discriminate muons arising from the prompt decay of boson from those produced in the decay of a hadron, the amount of deposited energy around the muon, or isolation, is defined in [13] as:

$$I_{PF}^{lep} = \frac{1}{p_T^{lep}} \left(\sum_{i}^{N_{h^\pm}} p_T^i + \sum_{j}^{N_\gamma} p_T^j + \sum_{k}^{N_{h^0}} p_T^k \right) \tag{30}$$

where the sum run over all the PF candidates without pile-up events: the charged hadrons (h), photons (γ) and neutral hadrons (h^0). This is going to be really important in the study of leptons produced in the electroweak decay of massive particles like Z or W bosons and for reject the leptons produced in jets decay. The isolated muons are those around which there is an energy deposited of less than 10% of its energy.

The muon reconstruction in CMS is very efficient. In Run 2 it was observed that this was an efficiency of essentially 100% in the tracker and more than 99% in the muon chambers.

4.1.2 Electron reconstruction

The electrons are reconstructed using the tracks of the tracker (Sec. 3.4.1) and the energies that have been deposited in the ECAL (Sec. 3.4.2). The intrinsic difficulty in the study of these particles is that electrons emit a large amount of energy as Bremmstrahlung radiation (photons) due to their low mass. For this reason, the emitted radiation must be recovered to reconstruct the initial transverse momentum of the electrons.

The so-called *isolated electrons* are reconstructed using the ECAL with the electron shower and those photons that appear to have been irradiated from the electron. All the showers are grouped together in what is called a *supercluster*.

The possible superposition of the electrons with other particles (non-isolated electrons) makes more difficult to reconstruct due to the possible existence of hadrons or photons that do not come from the electron. To do this, the trajectories of the tracker are used and associated them with ECAL clusters. To adjust the parameters coming from the tracker and the ECAL, an algorithm called *Gaussian-sum filter* (GSF) is used. Electrons are differentiated from isolated photons by looking for a no association between both sub-detectors (tracker and ECAL) information with the GSF algorithm. On the other hand, charged hadrons are differentiated by looking for energy depositions in the HCAL (Sec. 3.4.3).

The reconstruction efficiency of electrons is worse than that of muons. Using the tag-and-probe method, an efficiency of around 96% is observed.

4.1.3 Tau reconstruction

The tau (τ) is the heaviest Standard Model lepton and has a very short half-life of $\tau = (290.3 \pm 0.5) \cdot 10^{-15}$ s, due to which this particle decay before reaching the detector. To study or reconstruct these particles, the result of their decay must be observed, which can be leptonic or hadronic.

In the case of the leptonic decay ($\tau \to l + \nu_l$), it will be possible to identify a light lepton (e or μ) easy to reconstruct and a missing energy (MET) associated with the neutrino. On the other hand, there are many cases in which the decay channel is hadronic, which is called a *hadronic tau*, whose final state is made up of two quarks (two jets), such that $\tau \to q + q'$. This final state is difficult to reconstruct because these tau jets can appear to come from a direct quark or gluon decay. In order to identify them, it is used *hadron-plus-strips algorithm*, [15].

4.1.4 Jets reconstruction

Due to the strong interaction and color confinement phenomenon, coloured particles can only be found in bound states called hadrons. This type of grouping process is called *hadronization*. They form particles known as hadrons that are composed of quarks and the particle responsible for the strong interaction called gluon (g) which are the particles that suffer the strong force.

That's why this particles will produce a cascade of multiple strongly interacting particles along its propagation through the detector until the system reaches a state of equilibrium and with no isolated particles. For their study, physical objects called hadronic jets are created, which are formed of collimated particles. Jets include the leptons or photons produced as a result of a possible hadron decay. To analyze and study these jets, the *anti-k_T algorithm* is used.

This algorithm is based on the reconstruction of the jet in a cone with base radius R. The reconstruction criterion several variables into account, such as the energy ratio, the number of elements in the jet, and the number of charged and neutral particles in it. Once the general identification requirement is reconstructed, only those with $R \geq 0.4$ and the kinematic properties: $p_T > 25$ or $p_T > 30$ GeV (depending on analysis) and $|\eta| < 2.4$, are selected. For more detailed information on the anti-k_T algorithm, see [10].

4.1.5 Missing tranverse energy

It is a reality that some particles cannot be detected by the CMS, even with the complexity and completeness of its components. Among them can be considered: neutrinos or others unknown particles.

According to the conservation principle, the four-momentum in the initial state of a collision between two partons is expected to be conserved in the final state. By reconstructing the momentum of all the particles formed in the final state, it can be observed that the sum of all is different to zero. When that happens, it is associated with the presence of invisible particles that have not been detected. Mathematically it can be defined as the opposite of the sum in the transverse momentum of all particles formed in the final state:

$$\vec{p_T}^{miss} = -\sum_i p_T(i) \tag{31}$$

This missing transverse momentum of the events have to be measure clearly dependent on the reconstruction of all other event particles. It is usually called *missing tranverse energy* (MET).

4.2 Event simulation

The objetive of the measurement is to compare the experimental results obtained with the theory of the Standard Model to check if they have consistency with the theory, or also, if it is necessary to define new physics. For this, statistical studies of the Standard Model are used, based on simulations with MonteCarlo (MC) methods. All the setup used for MC generation is very complicated and has been prepared by the CMS. Simulations are performed in three different steps: generation, simulation and reconstruction. Below, will be explained how each of the processes is performed and what toolkits and programs are used for it.

For the generation of events, it is creates the initial conditions in which the collision occurs. Among this, it includes the PDFs (Sec. 3.1.2) and the theoretical cross sections of the different physical processes that want to be studied. Within the collision processes in the accelerator, interaction processes of physical interest (hard-process) or interactions of elastic collisions (soft-scattering) can occur. The generators are responsible for define a collision and keep in mind the probability of different final states according to the Standard Model. These randomly create the processes with the particles of the final state and their physical properties (momentum, pseudorapidity ...).

The main generators used are `Madgraph_aMCNLO` [4], `Powheg` [2], and `Pythia` [44]. The first two are responsible for generating hard-scattering events, while `Pythia` is the one that generates soft-scattering, hadronization, showers and possible radiations both in the initial state (ISR) and in the final state (FSR). Also, there is a toolkit called `Geant`, [1] for the simulation of the passage of particles through matter. It is used to simulate the transit of the generated particles across the different sub-detectors.

After generating the events according to the theory of the Standard Model and their passage through the different sub-detectors, the reconstruction of the physical objects and the event is carried out in a similar way to that proposed for the experimental data in Sec. 4.1.

PROCESS	TOOLS
WZ	`Pythia8`
ZZ	`Pythia8`
Non-prompt_DY	`Madgraph_aMCNLO`, `Powheg` and `Pythia8`
Non-prompt_TT	`Madgraph_aMCNLO`, `Powheg` and `Pythia8`
Non-prompt_VV	`Pythia8`

Table 1: List of processes that are going to be in this measurement with the tools used for their event simulation.

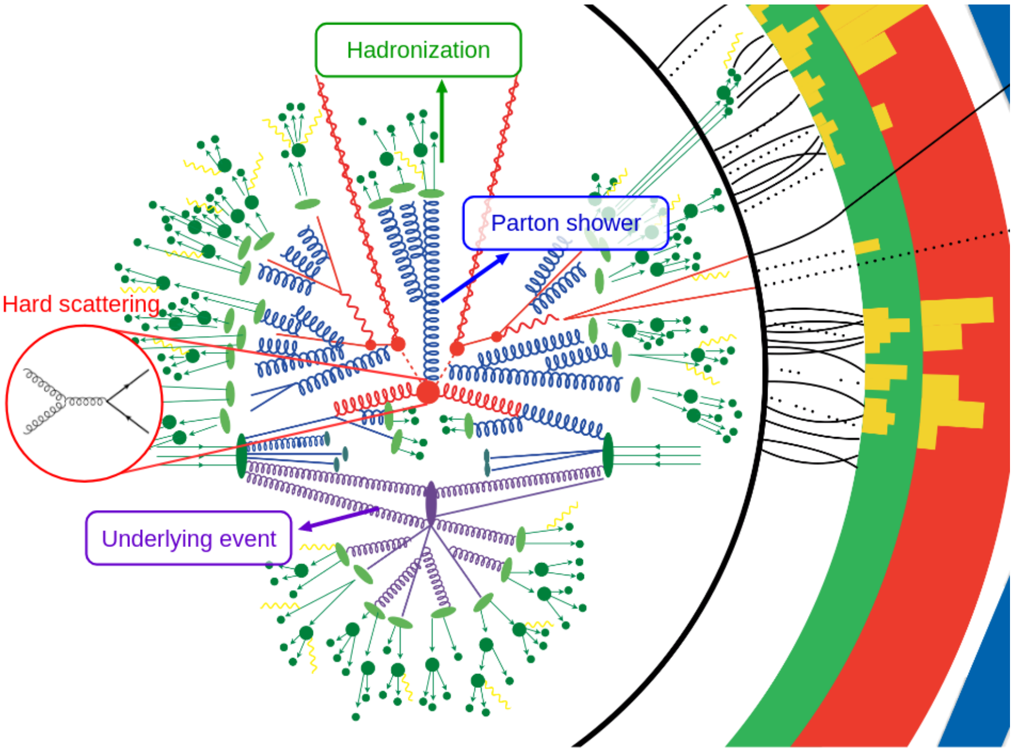

Figure 10: Schematic representation of a event simulation in proton-proton collisions. The red and blue circles represent hard scattering events and underlying events, respectively. The green dots, on the other hand, indicate showers as a consequence of hadronization.

5 Measurement of the WZ cross section

This section will explain the process used for the measurement of the cross section of the WZ production process using the experimental data obtained during the first year of Run 3 (2022) at an energy of $\sqrt{s} = 13.6$ TeV with a total luminosity of $\mathcal{L} = 29.36\ \mathrm{fb}^{-1}$.

5.1 Historical introduction

In the 1950s decade, with the approach of quantum electrodynamics, theoretical physicists dreamed on possible theories of unification between electromagnetic and weak interaction. The first indication of a possible merge of both forces was in 1973, when observations of neutrinos in cloud chambers concluded that it could only be explained by an intermediate particle that needs to be virtual, massive and electrically neutral. At that time particle accelerators did not reach energies so high as to generate these particles, so it was not until ten years later, that they were found.

In 1983, experiments performed UA1 and UA2 by proton-antiproton collisions at CERN's SPS accelerator would discover these particles. The mass of two mediator particles of the weak interaction could be predicted and measured for the first time. First, an electrically charged massive particle ($W^{\pm}$), subsequently, another massive neutral charge named by the grapheme Z. The processes observed in these experiments are those presented in Fig. 11. These studies gave strength to the theories that proposed a unification of both interactions.

These discoveries, in addition to being awarded the Nobel Prize in Physics in 1984, were a test that confirmed the hypothesis of a theory of unification of electromagnetic and weak interactions. In the last forty years, the study of the parameters of these particles and this theory have been an important discipline to study for particle physicists. These measurements and the discovery of the Higgs particle, [11], allow us to construct an electroweak theory within the Standard Model.

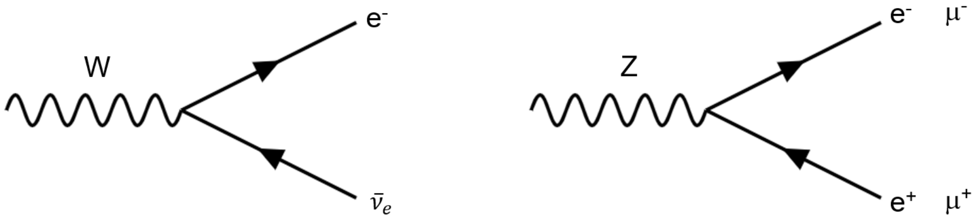

Figure 11: Feynman diagrams which show the different W^- and Z decays channel that was observed in their discoveries.

5.2 W, Z and diboson production

From an experimental point of view, the production processes of single W or Z have been studied in detail throughout the twentieth century. The W boson can have charge $q_e = \pm e$. That is why, according to the conservation of the charge, in its decay is expected to have the same electric charge. In addition, a quantity called lepton number is conserved. The final state of the decay can be two quarks or a charged lepton and a neutrino.

On the other hand, in the case of Z boson it is expected to have a final state with a neutral charge, conservation of lepton number and, in addition, the conservation of flavour. Therefore, the final state of the decay of a Z boson will be constituted by a fermion and its corresponding antifermion. The decay channels of W and Z can be seen in the Feynman diagram in Fig. 12.

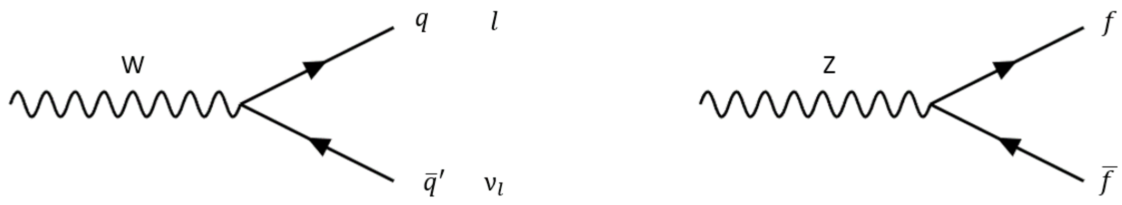

Figure 12: Feynman diagrams showing the possible decays of massive vector bosons. Although not explicitly included, charge and lepton number must be conserved in both processes. In addition, in the case of Z, the flavor must be conserved.

Nowadays, with the increase of the center-of-mass energy and the beginning of the study of proton-proton collisions, it has been possible to consider the access to new production channels of two vector bosons where we consider: WW, WZ and ZZ. The importance of these channels lies in a high sensitivity to new couplings to which a single vector boson does not have access. These are very important for studying Standard Model physics or accessing new physics.

For the study and reconstruction of events of these particles, final states formed by fermions will be obtained. Charged leptons (electrons and muons) are easy and precise to reconstruct in a detector, as they can be very well identified and their kinematic properties measured very accurately. On the other hand, quarks, due to the hadronization and hadronic showers (jets) produced, make their reconstruction difficult, which includes their identification and the measurement of their characteristics, not being as precise as they can be measured in charged leptons. For the study of the W and Z bosons, only the final state channels of leptonic decay will be studied in order to make the most reliable and precise measurement as possible. It is called: *multileptonic final states*.

5.3 WZ diboson production

This measurement focuses on the study of the production of WZ. This process, although it is not the one with the largest cross section, it has a relatively clean final state that will include three charged leptons, two coming from the Z and one from the W.

Furthermore, it is very interesting to suggest that it is possible to identify and tag the mother boson of the two leptons. The decay of Z occurs *on-shell*, so by observing the momentum of the leptons in the final state, flavour and charge, one can observe that two of them rebuild the mass of Z and have same flavour and opposite charge. The remaining lepton corresponds to W. This allows to reconstruct a very precisely final state and measure the properties of both bosons simultaneously.

Some of the contribution process of WZ production at leading order and next-to-leading order are shown in the Feynman diagrams of Fig. 13.

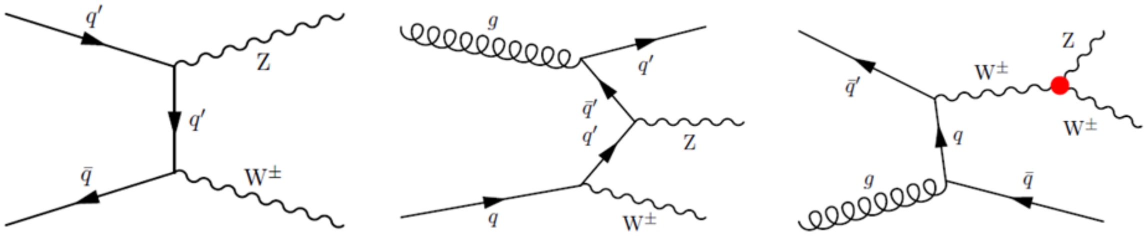

Figure 13: Representation of the Feynman diagrams of different WZ production contributions. The first two are diagrams at leading order (LO) in QCD in proton-proton collisions. The last shows a WWZ triple coupling (*red dot*) in a NLO in QCD, [32].

A characteristic of the WZ production is that it is sensitive to the *charge assymetry*. This channel can occur in two different ways: W^+Z and W^-Z depending on the sign of the charged boson. Due to interferences between the particles during the production of the event, processes can take place by which these two forms do not occur symmetrically, but there is a dominant state over the other. In other words, it can be appreciated if the distribution of events in processes W^+Z and W^-Z is not symmetric. Due to charge conservation in the production process, this asymmetry is associated with that of the initial state of the parton-parton collision, which allows us to access more information about the initial state of the process.

As described in 2.3, the masses of the W and Z particles are determined by the coupling with the Higgs boson. It is therefore interesting to consider what information about the Higgs we can extract from this process. By being able to make a simultaneous reconstruction of both W and Z bosons, it is possible to obtain information about their polarization state. The longitudinal polarization modes of massive bosons are a consequence of the Higgs scalar field. This is why, by studying the simultaneous polarization of both particles, the degree of polarization can be studied by observing the final state.

As mentioned above, dibosonic production channels are sensitive to some new couplings that cannot be studied in single boson processes. These channels can give rise to triple gauge coupling channels as shown in Fig. 2 and explained in Sec. 2.7. This WZ production channel allows obtaining information about the masses of the bosons by studying their coupling according to the equation Eq. 18. This type of coupling also allows the study of new physics.

To access this new physics and new particles proposed in theories such as SUSY, the energies that must be reached are too high to be accessible at the present. For this, the so-called *Effective Field Theory* (EFT) is used, a formalism that allows us to access this new physics and its effects through experiments at lower energies. This is based on the search of anomalous vertices and couplings that would not be allowed by the Standard Model or variations in expectations of SM existing channels. The triple coupling represents an access portal to the study of this type of process.

As partially mentioned in 3.1.2, the cross section is related to energy. This becomes visible in Fig. 14 where one can see the increase of the cross section of dibosonic processes with energy. The rate of increase of this amount can also be related to the partons distribution functions (PDFs) explained in 3.1.2. This type of process is purely electroweak, so cannot be given to leading order (Fig. 13) with gluons as partons in the initial state (gg), only with quarks (qq'). Production processes of two vector bosons with an initial state gg can only be given at next to leading order with an intermediate quark loop.

That is why these processes rarely occur like: $gg \rightarrow$ WZ. Looking at the PDFs of Fig. 6 we see that at higher energy gluon collisions are favored while qq' suffer slower growth. This is why the growth of the cross section for dibosons production processes is more subtle than others that grow more rapidly with energy such as the production of a quark top or a Higgs boson.

In addition, it is observed in Fig. 14, how this varies with the energy, adjusting a increasing curve. The cross section measurements comes from the results of different experiments put together.

Observing Fig. 15, it is possible to see the cross section ratios at different energies of these processes by comparing the experimental value obtained with the theoretical value. In the WZ process, the results obtained by the CMS at different center-of-mass energies are found in Tab. 7.

Energy	Cross section measurement (pb)
$\sqrt{s} = 7$ TeV	20.14 ± 1.32(stat.) $\pm$ 0.38 (theo) $\pm$ 1.06 (exp) $\pm$ 0.44 (lumi)
$\sqrt{s} = 8$ TeV	24.09 ± 0.87 (stat) $\pm$ 0.80 (theo) $\pm$ 1.40 (exp) $\pm$ 0.63 (lumi)
$\sqrt{s} = 13$ TeV	50.6 ± 0.8 (stat) $\pm$ 1.5 (syst) $\pm$ 1.1 (lumi) $\pm$ 0.5 (theo)

Table 2: Representation of all the measurement of the WZ cross section at different center-of-mass energies by CMS ([17], [27]). The uncertainties are included.

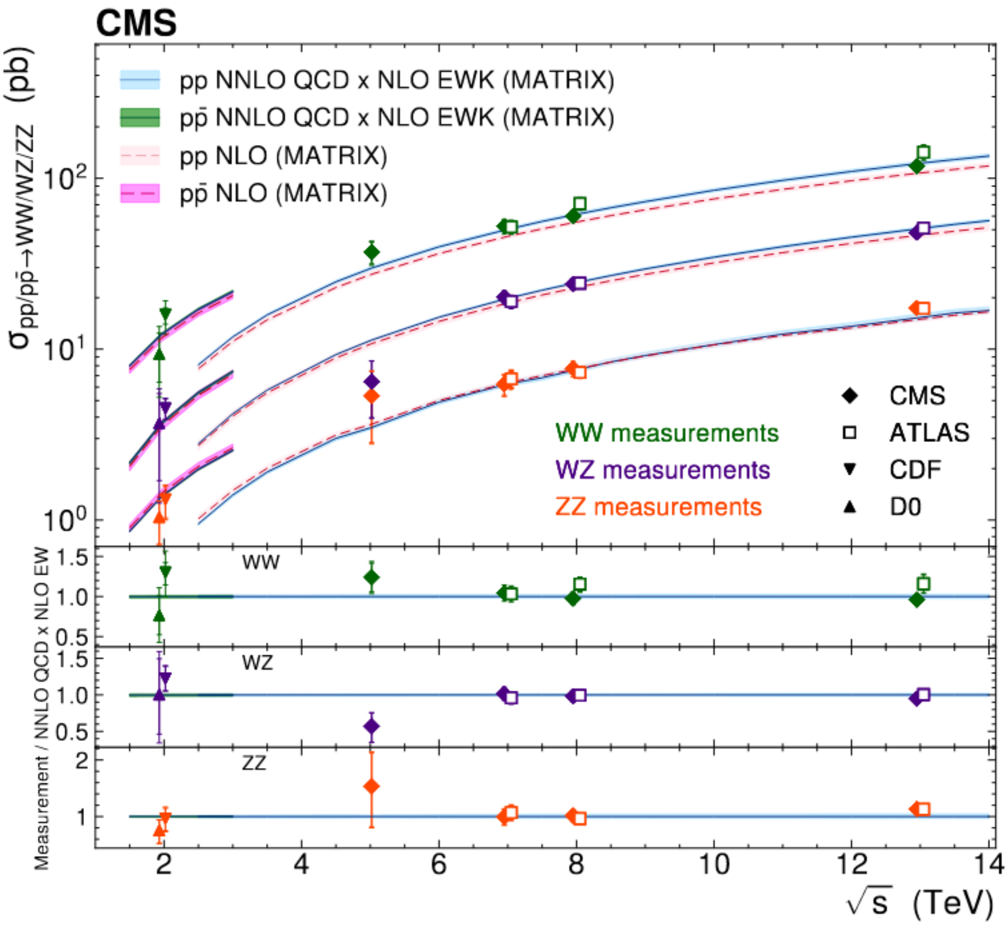

Figure 14: Measurement of the diboson production cross section at different center-of-mass energies for the CMS, ATLAS, CDF and D0, [18].

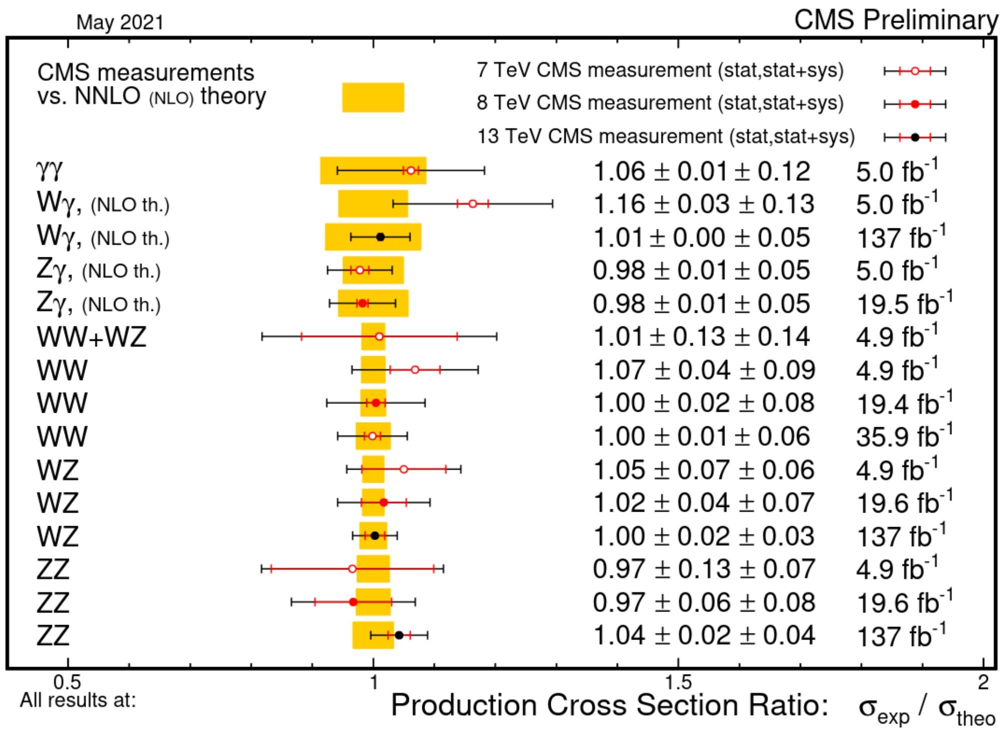

Figure 15: Measurement of diboson cross section and ratio comparison to the theoretical value, with measurement values taken at 7 TeV, 8 TeV and 13 TeV, [19].

5.4 Background description

In the SM there are different processes that recreate a final state that imitates the one we want to study from WZ. In this section, the processes that have been taken into account will be explained, but because for Run 3 many event simulation samples of some SM processes are not available, they will not be taken into account in this measurement. For more information about backgrounds in other WZ studies, could be consulted in [27].

5.4.1 ZZ background

This is a dibosonic process with a cross section of production lower than that of WZ production. Its main production channels are described in Fig. 16.

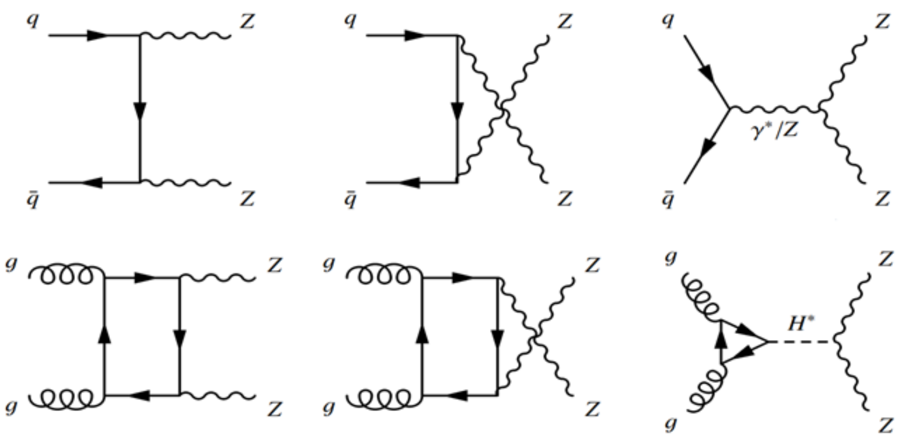

Figure 16: Feynman diagrams of ZZ diboson production process at leading order (LO) and next-to-leading order (NLO).

Similarly, the multileptonic final state will be made up of four leptons in total, two for each Z boson. Even so, there is the possibility that its final state is made up of only three leptons, according to what is expected in the final state of the WZ and may cause confusion. This could be due to the fact that one of the leptons of the decay of Z have low energy and does not reach the acceptance (assuming its energy as part of the MET) or it does not reach the selection requirements. Also, it could be that one of the bosons decays to a lepton τ and it decays into a light lepton and MET mimicking the final state of WZ.

5.4.2 Non-prompt background

There is the possibility of misclassifying particles due to a wrong interpretation of the results in the detector. For this reason, it is possible to take into account some processes in which, in a first moment, are associated with two leptons in the final state but there may be the presence of a non-prompt lepton. Among these processes we can include Drell-Yan (Fig. 17), $t\bar{t}$ pair production (Fig. 18) or VV production (with V a general vector boson W or γ).

The Drell-Yan process describes the production of lepton pairs in high-energy hadron-hadron collisions. This is achieved by quark-antiquark collision in which a very energetic γ or Z generates two leptons in the final state. Of course, there is the possibility that secondary radiations occur within the process, generating particles that can be identified as an extra lepton in the final state. These are what we call *DY-Non-prompt*.

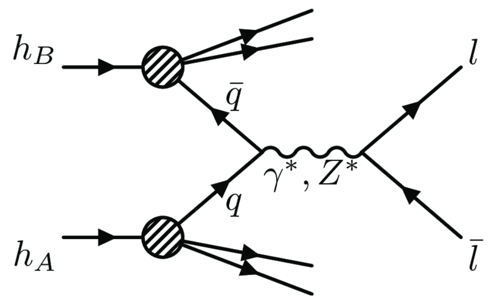

Figure 17: Feynman diagram of a general DY process where two quarks annihilate and create a pair of oppositely-charged leptons, [7].

On the other hand, the case of the production of top-antitop pairs is considered, see Fig. 18. This process has a high cross section and is easy to recognize due to its characteristic and well-defined final state. The top quark, due to the CKM matrix, Eq. 21, it is known that it practically always decays into a bottom quark (b) such that $t \to b + W^+$ where the boson W can have a final state of decay into two quarks or a lepton with a MET. Based on the decay channel of the W in the pair production process, we can consider: that both bosons decay into quarks (*hadronic*), that one decays into quarks and the other into leptons (*semileptonic*) and that both bosons decay in leptons (*dileptonic*).

If we consider the final lepton state, we have two leptons, 2 b-jets and some MET in the final state. If there is any non-prompt lepton and/or a bad identification of the b-jets can have a final state that mimics a WZ process. Although most top-antitop production cases would reconstructed correctly, but due to its high cross-section it must also be added as a background process.

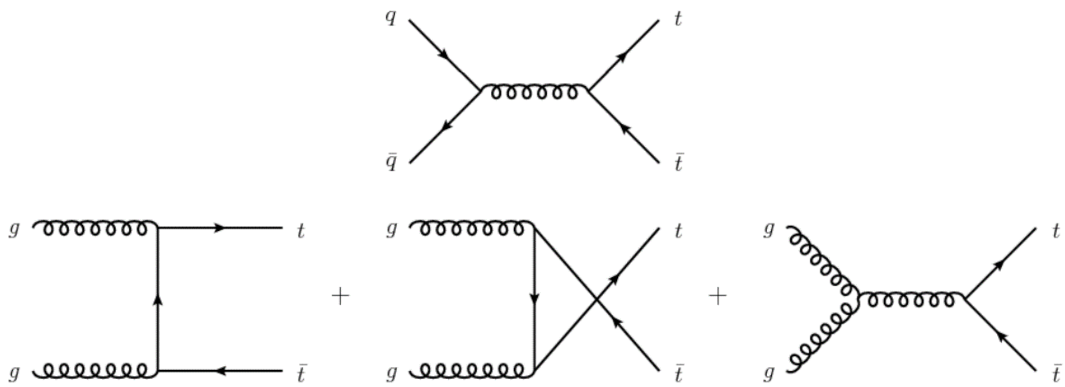

Figure 18: Feynman diagrams of $t\bar{t}$ production process at leading order (LO) with some different initial states.

5.5 Event selection

Events are selected using a trigger which requires some specific characteristics of the reconstructed objects to eliminate possible mis-identifications or to ensure a high efficiency of the measure.

5.5.1 Lepton identification

Leptons fulfilling certain quality criteria are used. Such criteria are chosen to achieve an identification efficiency of 96% in electrons and 99.8% in muons[4]. The criteria are summarized in Tab. 3 for muons and Tab. 4 for electrons.

[4]See more about electrons and muons efficiencies in [25] and [26].

Muon identification

Observable	Requirement	Observable	Requirement
p_T	> 10 GeV	d/σ_d	< 8
$\|\eta\|$	< 2.4	$\|d_z\|$	< 0.1 cm
$\|d_{xy}\|$	< 0.05 cm	Deep Jet of nerby jet	$<$ WP-medium
Isolation	$< 0.4 \times p_T$	PF muon	$>$ WP-medium

Table 3: All the object selection criteria for the case of Tight muons.

Electron identification

Observable	Requirement	Observable	Requirement
p_T	> 10 GeV	$\sigma_{i\eta i\eta}$	$< \{0.011/0.030\}$
$\|\eta\|$	< 2.5	H/E	< 0.10
$\|d_{xy}\|$	< 0.05 cm	$1/E - 1/p$	> -0.04
$\|d_z\|$	< 0.1 cm	Conversion rejection	✓
d/σ_d	< 8	Missing hits	$<$ WP-medium
Isolation	$< 0.4 \times p_T$	—	—

Table 4: All the object selection criteria for the case of Tight electrons.

The criteria are based on the measured values of p_T and the $|\eta|$ in the tracker. Furthermore, the distances $|d_{xy}|$ and $|d_z|$ will measure the distances to the vertex of the collision in the XY plane and in the Z axis respectively. It is also observed if these leptons are isolated according to what is explained in Sec. 4.1.1 and Sec. 4.1.2. There are also other criteria such as the width of the hits in the ECAL ($\sigma_{i\eta i\eta}$), the deposited momentum in the tracks of the tracker ($1/E - 1/p$) or the ratio of energies deposited between the HCAL and the ECAL (H/E).

5.5.2 Jet identification

Although the jets do not have a directly important role in the WZ process when studying channels with a multilepton final state, it is interesting to identify these objects and classify them for the study of other processes. In this case, it is important for the study of background events. The reconstruction of jets, as mentioned in Sec. 4.1.4, is carried out with an algorithm called anti-k_T in charge of collecting all the particles coming from the showers and within a cone-shaped cluster.

Its identification is very complicated, but it is interesting to know from which particles certain showers come from, which will allow us to separate certain backgrounds. First of all, pile up clusters are removed by a new algorithm introduced in Run 3 called *Pileup Per Particle Identification* (PUPPI), [8]. On the other hand, the jets coming from b quarks are identifiable by the DeepCSV algorithm [24]. The jets identification efficiencies is approximately 90%. The b-tagging algorithm is around 70%.

5.5.3 Signal Region

In order to study a specific process of the Standard Model, it is considered a set of event selection criteria that allows us to identify and select all the events of the given process. These requirements will consist of a amount of characteristics of the final state of the WZ process that was reconstructed in the detector. When working with selected events in the production channel, it is called *Signal Region* (SR).

The signal region will be defined by the final state of the production process of two WZ vector bosons. As mentioned in Sec. 5.2, this will be defined by three leptons in the final state and one missing transverse energy.

The three leptons will use the tight leptons (consult Tab. 4 and Tab. 3) criterion in order to make their identification very precise. It is also known that two of these leptons come from the decay of the Z boson, where these two will be characterized by having opposite sign and same flavor (OSSF). Furthermore, studying the invariant mass of these two leptons ($m_{ll'}$) approximates the mass of the Z boson (m_Z). These two leptons will be tagged as *Z leptons* (l_{Z1} and l_{Z2}). The remaining lepton will be associated with the one coming from the W boson.

The transverse momentum of the leptons coming from Z is imposed to have $p_T^{l_{Z1}} > 25$ GeV and $p_T^{l_{Z2}} > 10$ GeV. The lepton coming from the W boson is required to have $p_T^{l_W} > 25$ GeV. Furthermore, we want the invariant mass of the OSSF lepton pair to satisfy $m_{ll'} > 4$ GeV to eliminate low energy resonances that can contaminate the event and more specifically, that it approaches the Z mass with a small difference such $\Delta m < 15$ GeV. The total invariant mass of the three leptons must be $m(l_{Z1}, l_{Z2}, l_W) > 100$ GeV. To be able to reconstruct the WZ, a MET that have at least $p_T^{miss} > 30$ GeV is required. No b-jet are expected in the process ($N_b = 0$).

- 3 tight leptons ($N_l = 3$).
- At least 1 pair of opposite sign and same flavour ($N_{OSSF} \geq 1$) and no b-tagged jets ($N_b = 0$).
- Transverse momentum: $p_T^{l_{Z1}} > 25$ GeV, $p_T^{l_{Z2}} > 10$ GeV, $p_T^{l_W} > 25$ GeV and $p_T^{miss} > 30$ GeV.
- Invariant mass: The OSSF leptons pair (l_{Z_1} and l_{Z_2}) must have a invariant mass of at least $m_{ll'} > 4$ GeV and $|m_Z - m_{ll'}| < 15$ GeV. The invariant mass of the three leptons has to be $m(l_{Z1}, l_{Z2}, l_W) > 100$ GeV.

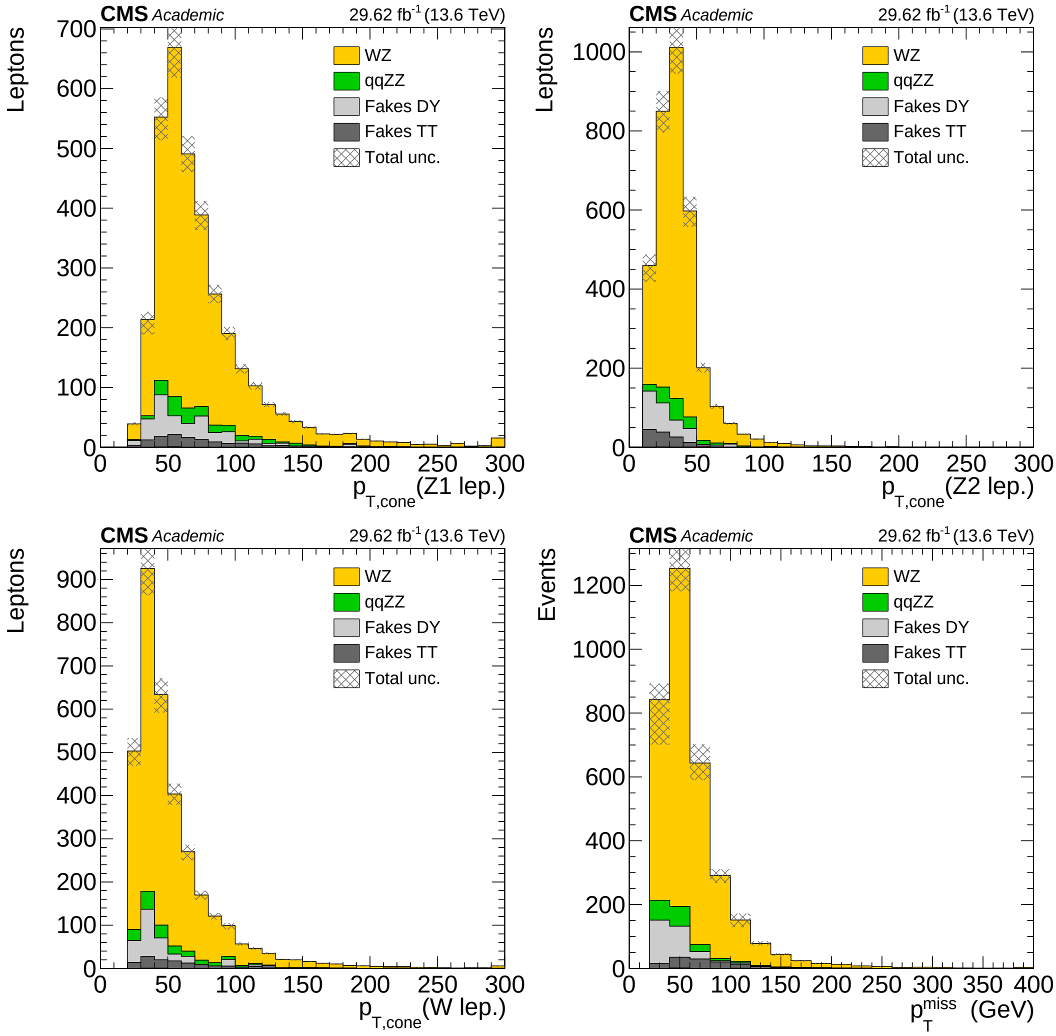

Figure 19: Total events at different transverse momentum for the first and second boson Z leptons, the W lepton and the reconstruction of the missing transverse energy This figures are representations of the events in signal region with the MC samples.

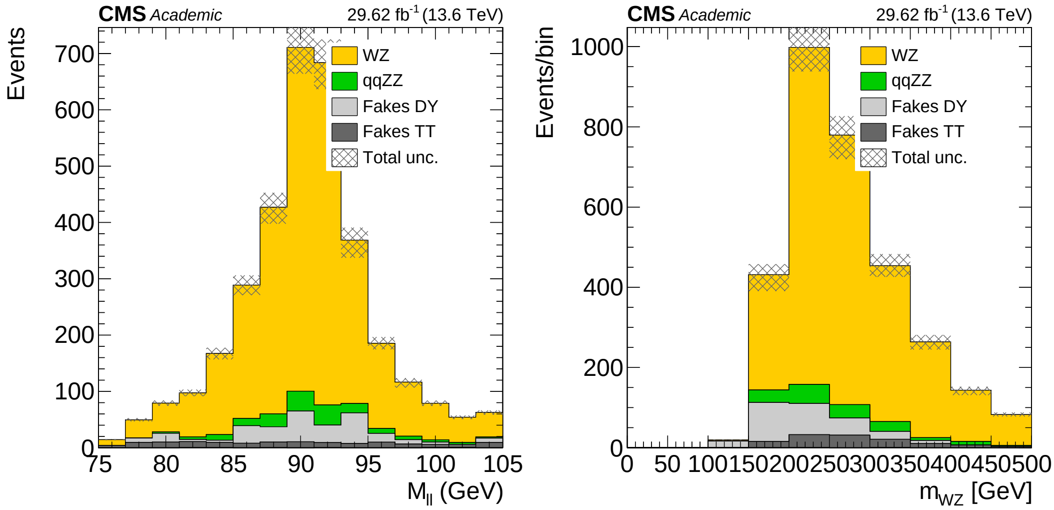

Figure 20: Total events for the reconstruction of the invariant mass in the signal region with the MC samples. First, with the two leptons l_{Z1} and l_{Z2} whose invariant mass shows us the resonance around the mass of the Z boson. The second shows the reconstruction of the invariant mass of the three leptons and the missing transverse energy for reconstruct the invariant mass of the two W and Z bosons.

It is possible to see in Fig. 19 and Fig. 20, the results after defining the selection criteria for the studied process. It was obtain the presence of others different process from the SM that makes the signal region not pure. These contributions are what were called: *background processes*.

5.5.4 Control Regions

In order to estimate the different backgrounds as accurately as possible, new regions are defined with the goal of maximizing the number of events for a particle background process and study it in detail regardless of the signal region to check the good estimation of backgrounds. It is called: *Control region* (CR). In this measurement, two different control regions are used. First, is used a control region based on the ZZ background and later, the top-antitop pair production control region is defined as well.

For maximize the ZZ production process (CR-ZZ) where 4 well-defined leptons are required in the final state, the identification and tagging of leptons is very similar to that carried out in SR, where it is possible to generate two pairs of opposite sign and the same flavor that make it possible to identify which boson are associated to the four leptons. It is also based on the invariant mass by pairs. In this case, since there is no W boson, no missing transverse energy is required and no b-jet is expected. The transverse momentum requirements of the leptons is analogous to that used for the Z leptons of the signal region.

- 4 tight leptons ($N_l = 4$).
- At least 1 pair of opposite sign and same flavour ($N_{OSSF} \geq 1$) and no b-tagged ($N_b = 0$).
- Transverse momentum: $p_T^{l^1_{Z1}} > 25$ GeV, $p_T^{l^1_{Z2}} > 10$ GeV, $p_T^{l^2_{Z1}} > 25$ GeV, $p_T^{l^2_{Z2}} > 10$ GeV and $p_T^{miss} = 0$ GeV.
- Invariant mass: The OSSF leptons pair must have a invariant mass of at least $m_{ll'} > 4$ GeV and $|m_Z - m_{ll'}| < 15$ GeV. The invariant mass of the three leptons has to be $m(l_{Z1},\, l_{Z2}, l) > 100$ GeV.

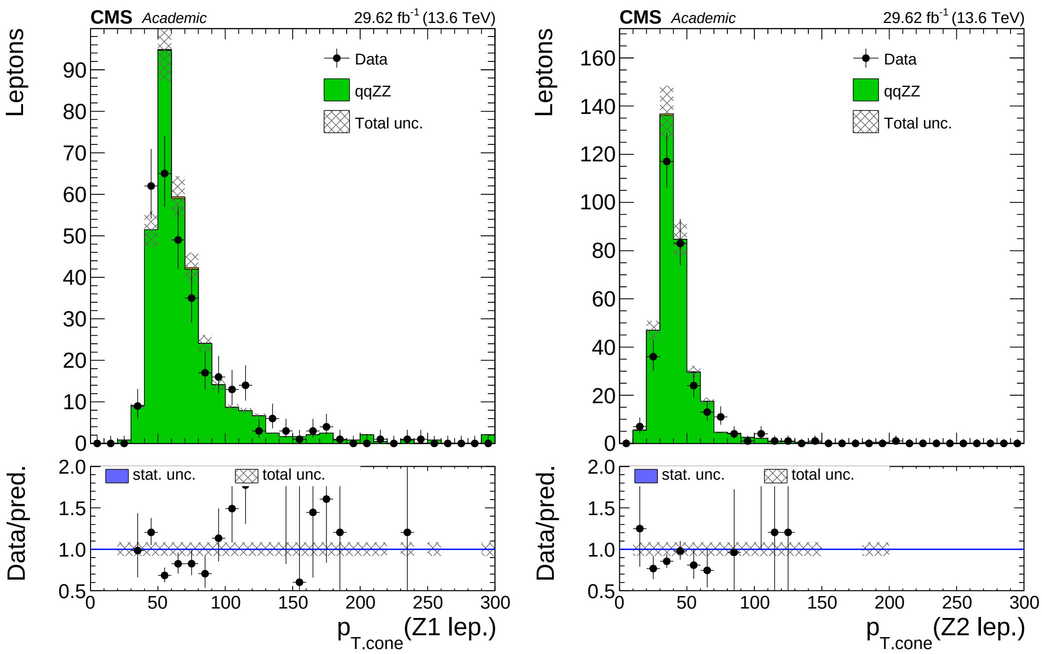

Figure 21: Total events at different transverse momentum for the first and second lepton and the reconstruction in the ZZ control region with data and the MC samples.

In other hand, for maximize the top-antitop production process (CR-TT) the conditions are quiet different. If we recall what was explained in Sec. 5.4.2, the top-antitop process will be characterized by having two b-jets associated to the decay of the top quarks and two W bosons of opposite sign. It is being studied the leptonic decay channel, so it is expected that the decay of the two W bosons will result in two leptons of opposite sign and a missing transverse energy associated with two neutrinos. Testing different cuts to maximize this process, it has been concluded that:

- 2 tight leptons ($N_l = 2$).
- No pair of opposite sign and same flavour ($N_{OSSF} \geq 0$), $N_{jet} > 1$ and b-tagged jets ($N_b \geq 1$).
- Transverse momentum: $p_T^{l_1} > 25$ GeV, $p_T^{l_2} > 20$ GeV and $p_T^{miss} > 30$ GeV.

- Invariant mass: A invariant mass of at least $m_{ll'} > 12$ GeV.

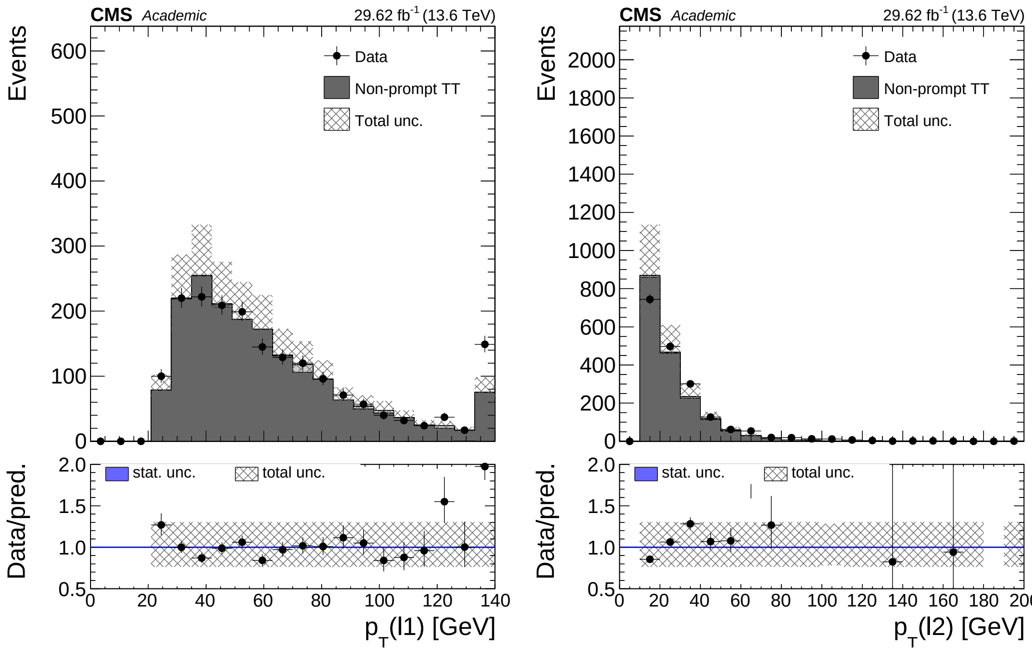

Figure 22: Total events at different transverse momentum for the first and second lepton in the $t\bar{t}$ control region with data and the MC samples.

5.6 Systematic uncertainties

One of the most important parts of the measurement and results is the measurement of some parameters associated with the results that measure the degree of dispersion in the results taking into account all the variables associated with the experiment. Two types of uncertainties are taken into account: systematic and statistical. The statistical uncertainty is associated with the amount of data that make up the sample. Since the LHC just started working at $\sqrt{s} = 13.6$ TeV just one year ago, the statistic available is limited to $\mathcal{L}_{13.6\ \mathrm{TeV}} = 29.62\ \mathrm{fb}^{-1}$ currently, while for example in Run 2 after three years of data collection, there was a total of $\mathcal{L}_{13\ \mathrm{TeV}} = 138\ \mathrm{fb}^{-1}$. The Run 3 data should increase significantly for the next few years.

Systematic uncertainty is properly associated with the design of the experiment and possible variables that are beyond the current control of the design. Some of this uncertainties are associated with: the operation of the collider, the detector, the trigger, modelling in the event simulation sample generators, theoretical and others. The available systematic uncertainties will be described below:

- **Luminosity:** It is associated to the MonteCarlo sample normalization in relation with the available data of $\mathcal{L}_{13.6\ \mathrm{TeV}} = 29.62\ \mathrm{fb}^{-1}$ taken during 2022. This uncertainty affects the measurement by 2%.

- **Jet energy scales:** These are possible uncertainties related with the estimation of jets characteristics in their reconstructions such as: momentum, pseudorapidity or energy.

- **Background normalization:** It is an uncertainty associated to the normalization of the simulated background events applied in the signal region. These normalizations float freely in the fit as an unconstrained nuisance parameter. It is going to be study in detail in Sec. 6.2 and Sec. 6.3.

- **Muon and electron efficiencies:** These are uncertainties related with corrections made to increase the efficiency in the Monte Carlo simulations by taking some statistical weights. It creates a greater similarity between the experimental data and the sample of simulated events.

- **ISR and FSR:** The uncertainties associated to the Initial State Radiations (ISR) and the Final State Radiations (FSR). These are associated with the possible radiation emission of particles on the initial/final state which generates objects in the detector that are going to be tagged. For example: emission of photons, quarks or gluons that deposit jets and showers in the different calorimeters. All the corrections associated with this possibilities are included in this uncertainties.

There are many other existing systematic uncertainties that are not available yet for the Run 3 analysis. For the further analysis and other future studies, it should be available.

5.7 Signal extraction and maximum likelihood fit

There are different methods to measure the cross section in particle physics. For obtain the cross section of a given process, would only have to count the number of events that exist, but the background processes contaminate the sample and their contributions have to be consider. This can be calculated using Eq. 32.

$$\sigma = \frac{(N_s - N_{bck})}{BR \cdot L \cdot \mathcal{A} \cdot \varepsilon} \tag{32}$$

The objetive is to estimate the rate between the measure of an experimental cross section and the expected from the SM. It is called *signal strength*.

$$r = \frac{\sigma_{exp}}{\sigma_{SM}} \tag{33}$$

The signal extraction could be studied extracting the number of events per bin in a selected distribution which allows to separate correctly the signal for the background and study the yield of it.

$$y_i = \vec{r} \cdot N_s + N_b \tag{34}$$

where N_s are the number of signal events and N_b are the background events. The $\vec{r}$ is group of parameters used to extract the signal strength of the signal. This parameters are called *parameters of interest* (POIs).

For the estimation of the POIS is used a *Maximum Likelihood* fit (ML fit). It is a parametrization for fit and estimate parameters using observables information. Fixing all the parameters is possible to define a function called *Likelihood function*:

$$\mathcal{L}(\vec{r}, N_s^i(\theta^i),\, N_b^i(\theta^i)) = \prod_{i=1}^{N_{bins}} Pois(n_i|\vec{r}\cdots(\theta) + N_b(\theta)) \prod_{k}^{N_{uncs}} e^{\frac{\theta_j^2}{2}} \tag{35}$$

where n_i is the data per bin, θ is a vectorial collection of parameters and $Pois$ is a Poisson probability density function defined like:

$$Pois(n_i|\vec{r}\cdots(\theta) + N_b(\theta)) = \frac{1}{n_i}(r \cdot N_s^i(\theta) + N_b(\theta))e^{-(r \cdot N_s^i(\theta) + N_b(\theta))} \tag{36}$$

At the end of the process, the amount of events corresponding to the signal process can be extracted from the MC and the cross section could be measured. A toolkit has been used for this measurement called `Combine`[5].

5.8 Measurement procedure

Due to CMS policies and to avoid possible bias in the results, at the beginning the measurement was done without making use of the experimental data in the signal region. In it, only Monte Carlo simulations was used. On the other hand, the control region can use these experimental data, which will allow us to study the background processes in detail. The data in signal region was only implemented when the full analysis was completed.

In this subsection, it is presented the process for the measuring of a cross section of WZ production process with the signal extraction from using maximum likelihood fit in control regions. For this, a thorough study of ZZ and $t\bar{t}$ control regions in order to extract the signal and reduce the uncertainties associated to their normalizations.

[5] More information could be found in https://cms-analysis.github.io/HiggsAnalysis-CombinedLimit/

6 Results

6.1 Signal Region interpretations

In the signal region, it is used the event selection of 5.5.3 for the representation of an enriched in WZ process distributions. It can be seen in the distributions of Fig. 23 and Fig. 24 that are enriched in the WZ process and that they satisfy the requirements in the transverse momentum of the leptons and the missing transverse energy. The Fig. 24 shows the invariant mass. The one on the left, shows the invariant mass of the two leptons associated with Z, so we see that the maximum of the mass distribution is around the mass of the Z boson (m_Z). On the other hand, the graph on the right in Fig.24 shows the invariant mass of the three leptons and the MET, so the mass of the two bosons (W and Z) is being reconstructed. That is why the maximum of the distribution is around $m_Z + m_W$.

At first, in the measurement, data in the signal region was not used, so the signal was fit in Asimov distribution that consists of putting the data the same as the MonteCarlo. This directly implies that the cross section is being considered equal to that of the Standard Model. In the end, the data was implemented to repeat the measurement and obtain the value of a real cross section. As can be seen in Fig. 23 and Fig. 24, there is good agreement between the data and the MC simulations.

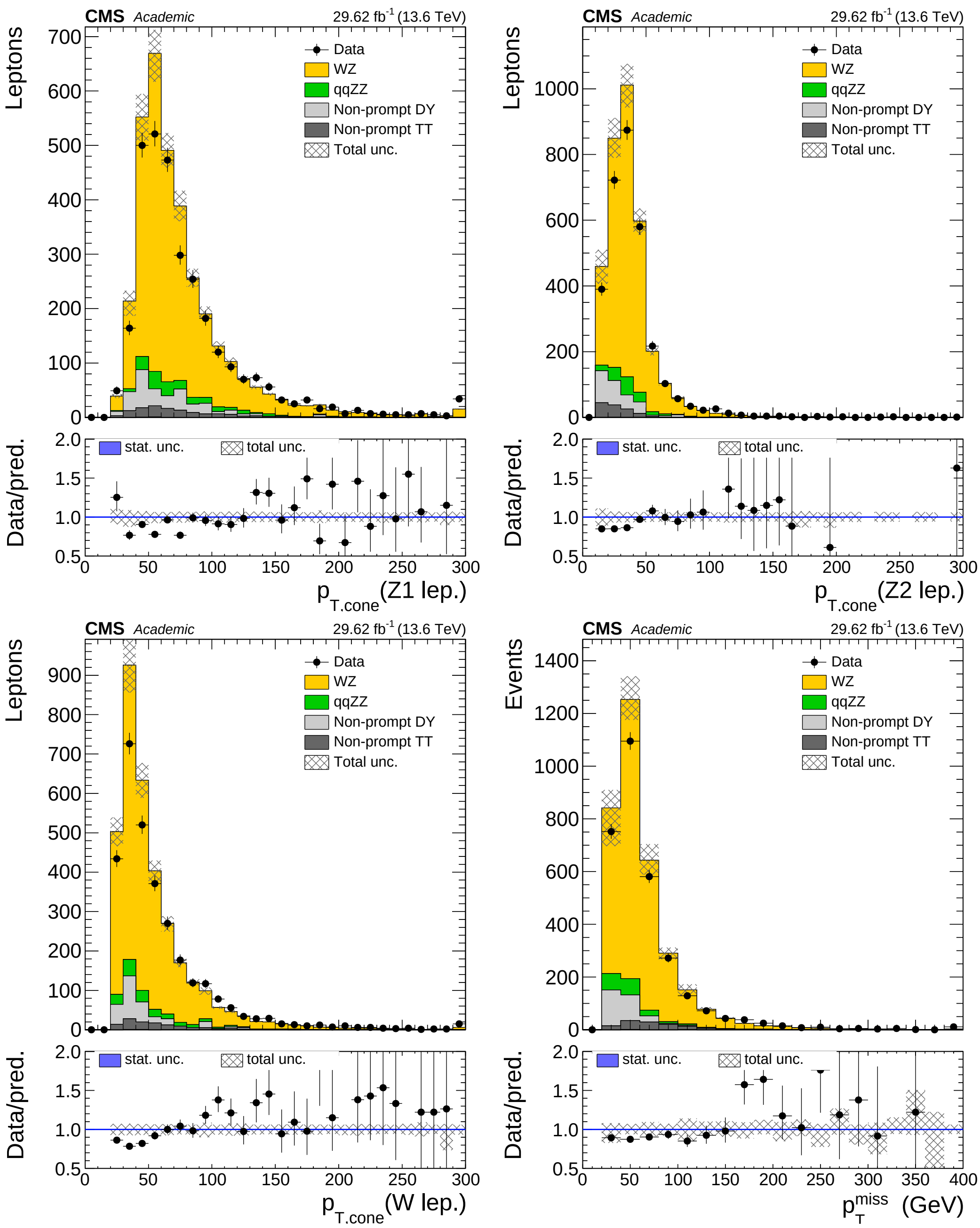

Figure 23: Total events at different transverse momentum for the first and second boson Z leptons, the W lepton and the reconstruction of the missing transverse energy This figures are representations of the events in signal region with the MC samples and data.

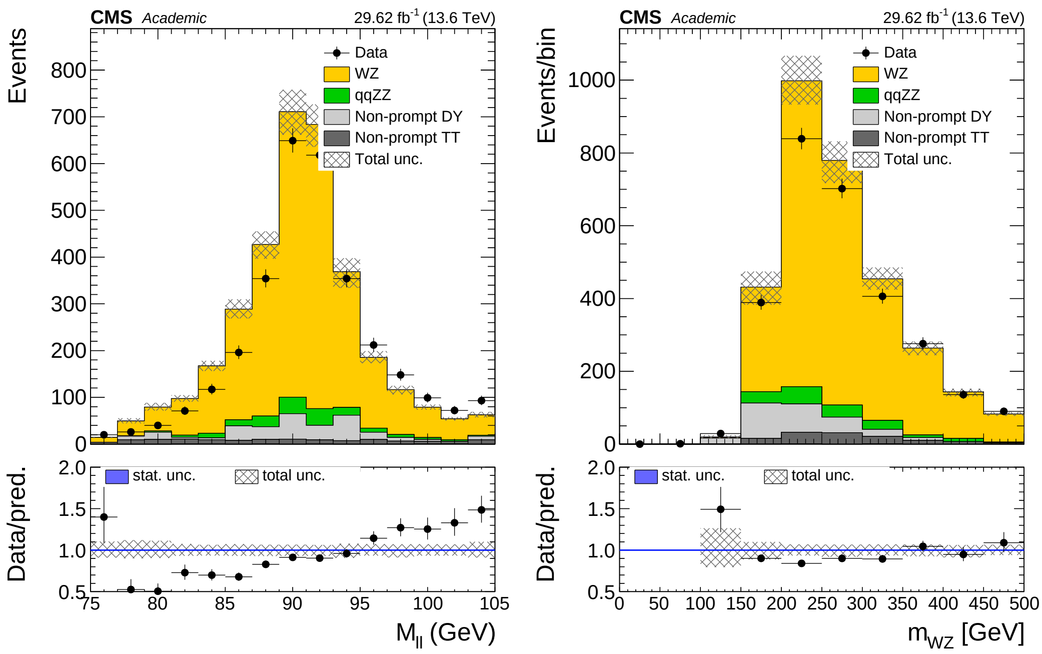

Figure 24: Total events for the reconstruction of the invariant mass in the signal region with the MC samples and data. First, with the two leptons l_{Z1} and l_{Z2} whose invariant mass shows us the resonance around the mass of the Z boson. The second shows the reconstruction of the invariant mass of the three leptons and the missing transverse energy for reconstruct the invariant mass of the two W and Z bosons.

6.2 ZZ Control Region analysis

The ZZ control region is used to measure the cross section of the WZ production process and its uncertainties. In Fig. 33, it can be seen how in the control region of ZZ the background is so negligible that it does not exist and its distributions are independent of the signal region. In addition, we can see that there is a good agreement between the experimental data and Monte Carlo since they fall within the uncertainties in all the bins. It is true that if we had more data samples, it is likely that the results would fit even better.

For the signal extraction, it will be used the control distribution region of ZZ that best fits with the data. In addition, a distribution that does not depend on the kinematic variables will preferably be chosen. Finally, it was decided to use the lepton flavor distributions to get a fit of the signal region and the control region of ZZ.

The signal is extracted from a fit to distributions of Fig. 25 in the signal region and the ZZ control region where the normalizations of WZ and ZZ are extracted simultaneously in the fit. After including simultaneously the $t\bar{t}$ control region to the fit explained in Sec. 6.3, the results of the signal extraction and the maximum likelihood fit with all the impacts of the uncertainties are shown at the end in the Sec. 6.

Process	eee	$ee\mu$	$e\mu\mu$	$\mu\mu\mu$
Signal WZ	445 ± 10	553 ± 11	778 ± 13	1053 ± 15
qqZZ	21 ± 10	35 ± 4	39 ± 4	71 ± 5
Non-prompt DY	47 ± 14	19 ± 9	132 ± 23	66 ± 16
Non-prompt TT	12 ± 1	24 ± 2	38 ± 2	50 ± 3
Non-prompt VV	0.4 ± 0.3	0.2 ± 0.2	0.9 ± 0.4	0.0 ± 0.0
Data	456	547	869	1197

Table 5: The distribution of MC sample and data classified per bin using the lepton flavour criteria in the signal region.

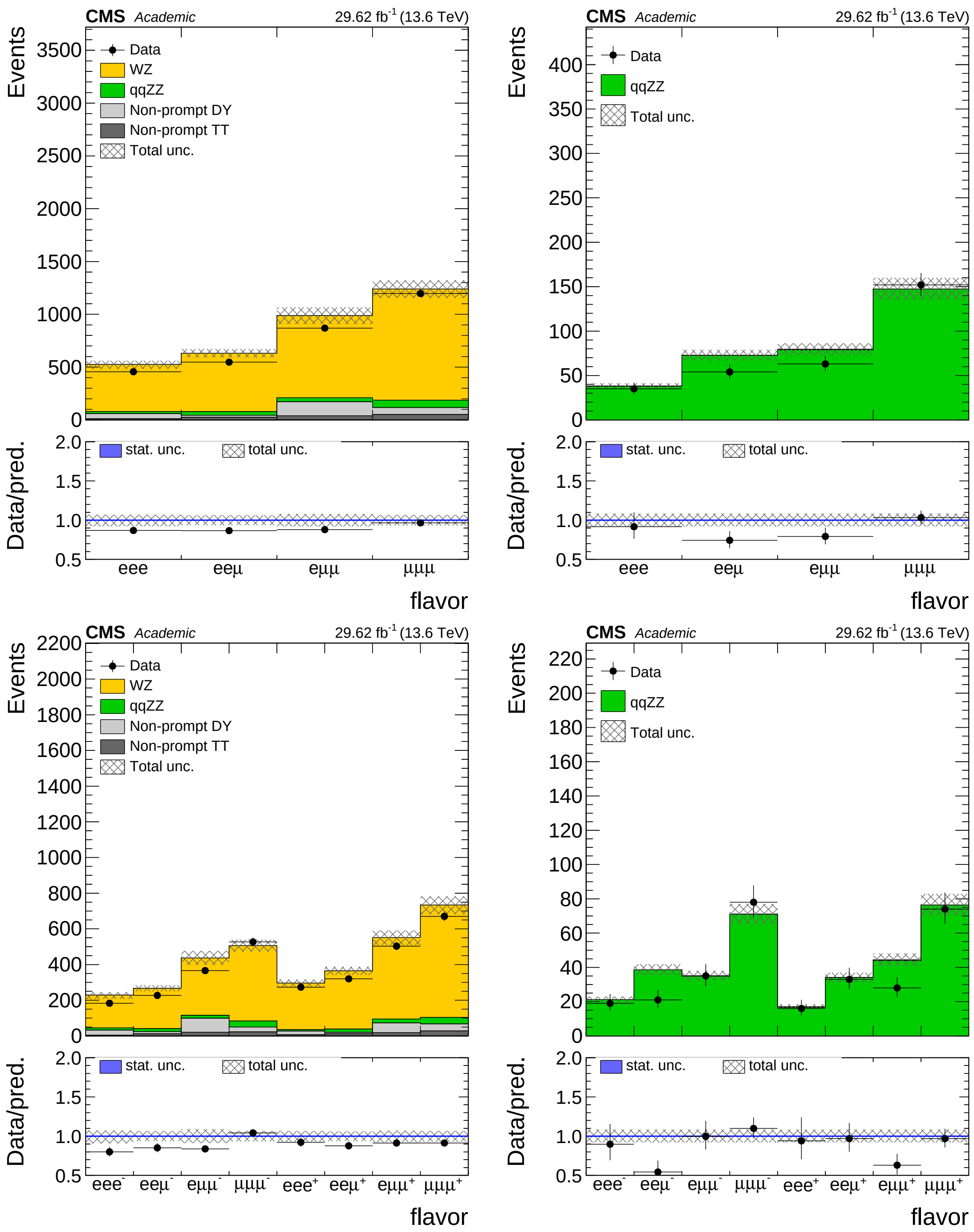

Figure 25: Total events distribution of leptons per flavour and distribution of leptons flavour and charge in both: signal region and the ZZ control region.

6.3 $t\bar{t}$ Control Region analysis

After event selection to obtain a control region enriched in the non-prompt background of top-antitop pair production, it is searched in a similar way to what was done in the control region of ZZ. The objective is to add also a normalization of the non-prompt $t\bar{t}$ control region with the signal region of WZ and the control region of ZZ. It also allows us to constrain (reduce) the uncertainty associated to the normalization of this background.

The distribution of the transverse momentum associated to the Fig. 26 is the one that best fits the MonteCarlo simulation to the data. For this reason, it is the one used to extract the normalization of the top-antitop non-prompt in the signal extraction. We can see the result of this normalization in Sec. 6.

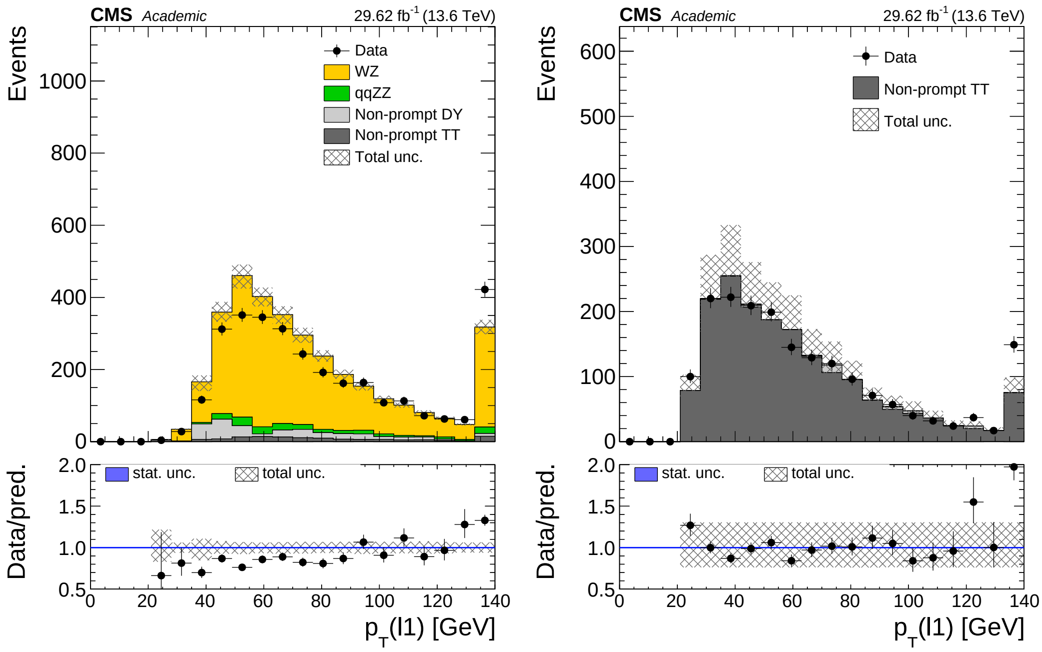

Figure 26: Total events distribution of momentum of the more energetic lepton in the the signal region and the top-antitop control region where data is used.

Process	Number of events
WZ	2828.48 ±24.06 (stat.) ±171.63 (syst.)
qqZZ	165.25 ±8.28 (stat.) ±16.57 (syst.)
Non-prompt DY	264.58 ±32.09 (stat.) ±31.58 (syst.)
Non-prompt TT	124.40 ±4.37 (stat.) ±7.35 (syst.)
Non-prompt VV	1.54 ±0.58 (stat.) ±0.09 (syst.)
Data	3069

Table 6: The total events of MC sample and data distributions of the momentum of the more energetic lepton in the signal region.

6.4 Expected results

Before adding the data in signal region, the influence of the different systematic unceratinties to our measurement is calculated.

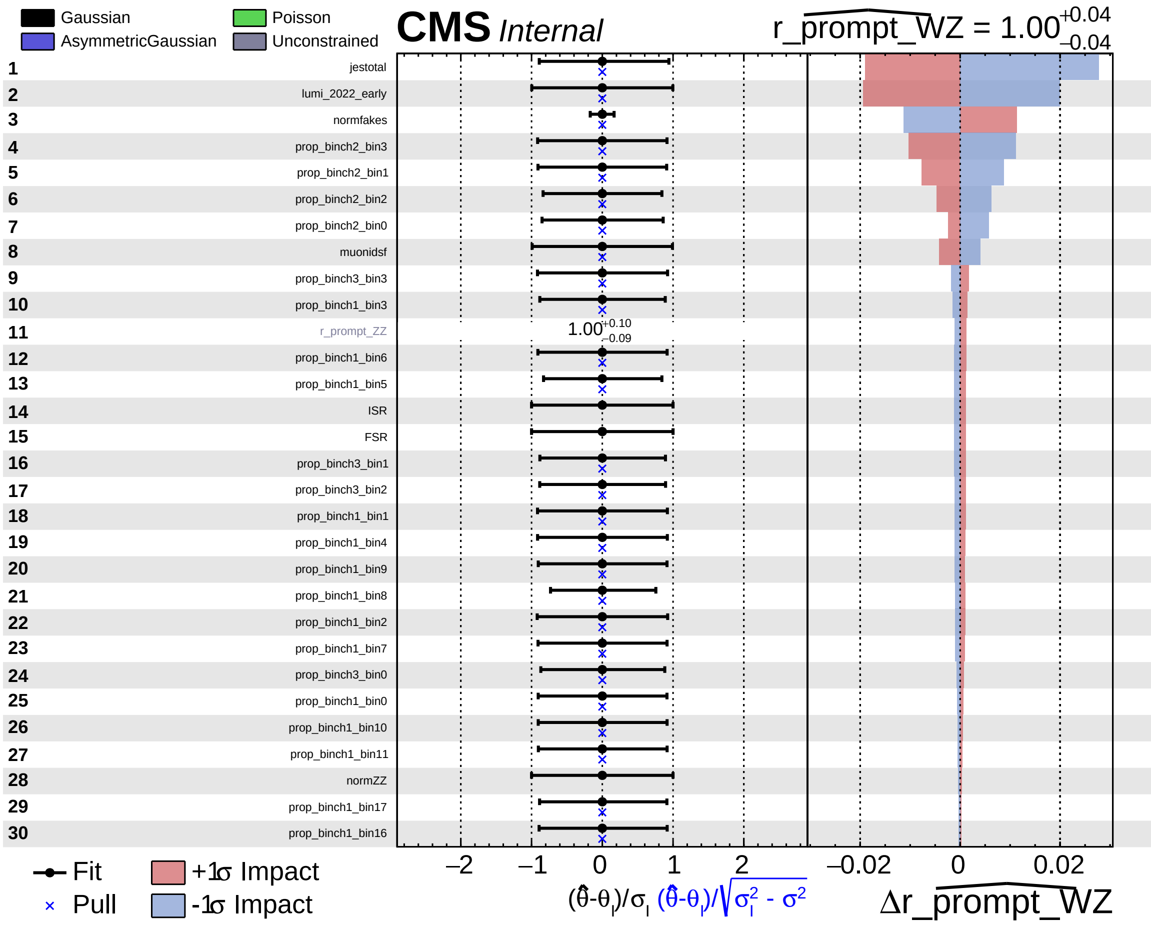

Figure 27: Impact of the different source of systematic uncertainty available for the Run 3 with no data in the WZ signal.

The Fig. 27 shows the value of impact of a nuisance parameter (NS) on the POIs described in Sec. 5.7. In other words, it is possible to measure the influence of these parameters on our measurement uncertainties, to know how they affect our results.

On the right it can be seen that a high value of $\pm 1\sigma$ implies a large impact and a high contribution to uncertainty. On the left, are the initial values of the NS and the post-fit values with the error bars.

In Fig. 27, it can be seen that although the value of the NS is set to zero, the variation in the error bars is observed. It can be seen how the normalization *normfakes* associated with the *non-prompt* backgrounds are highly constrained thanks to the fit studied with the $t\bar{t}$ background. In the part on the right, it can be seen that what generates the greatest impact in the measure are the jet energy scales and the luminosity. Those associated with muon efficiencies and others associated with statistical variables, ISR or FSR are also appreciable in smaller contributions.

A signal strength value with its uncertainties is shown at the top of the graph. In this specific case, having fixed the value of the data to MonteCarlo, the result is $r = 1.00$, but it is of interest to observe the uncertainty of ± 0.04, which is quite an expected value according to previous measurements.

Finally, after defining all the sources of uncertainties and extract the signal strength, it is possible to obtain the validity of our measure using a likelihood fit scan (Fig. 28).

It is a logarithmic representation of the likehood function where the horizont lines in $-2\,\Delta\, ln\, L = 1$ and $-2\,\Delta\, ln\, L = 4$ represent a 68% and a 95% of confidence in our measure, respectively. The black curve represents the joint of all the systematic and statistic available uncertainties in the Run 3 dataset. The red curve represent the statistical uncertainties which are freeze.

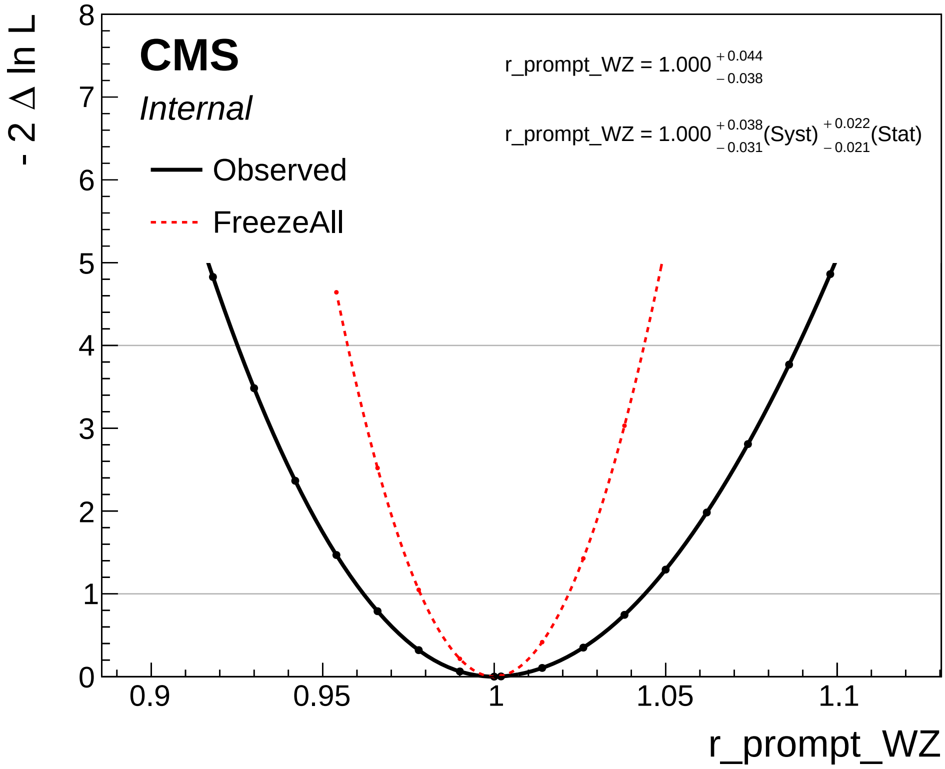

Figure 28: The fit ratio for the measurement of the expected WZ production cross section using the 2022 data from the CMS.

This Fig. 28 guarantees that the sum in quadrature of the individual components is equal to the total uncertainty. It is possible to obtain the statistical and systematic uncertainties associated with the measurement made.

$$r_{wz-asimov} = \frac{\sigma_{exp}}{\sigma_{SM}} = 1.00 \ {}^{+0.038}_{-0.031} \ (Sys) \ {}^{0.022}_{0.021} \ (Stat) \tag{37}$$

With this we can have an estimate of what the results are like in a first approach to the measure of an expected cross section an its uncertainties.

6.5 Observed results

The impact of uncertainties in the cross section measurement is extracted from the signal regions and using the information of the two control regions (ZZ and non-prompt $t\bar{t}$) using now the data in signal region.

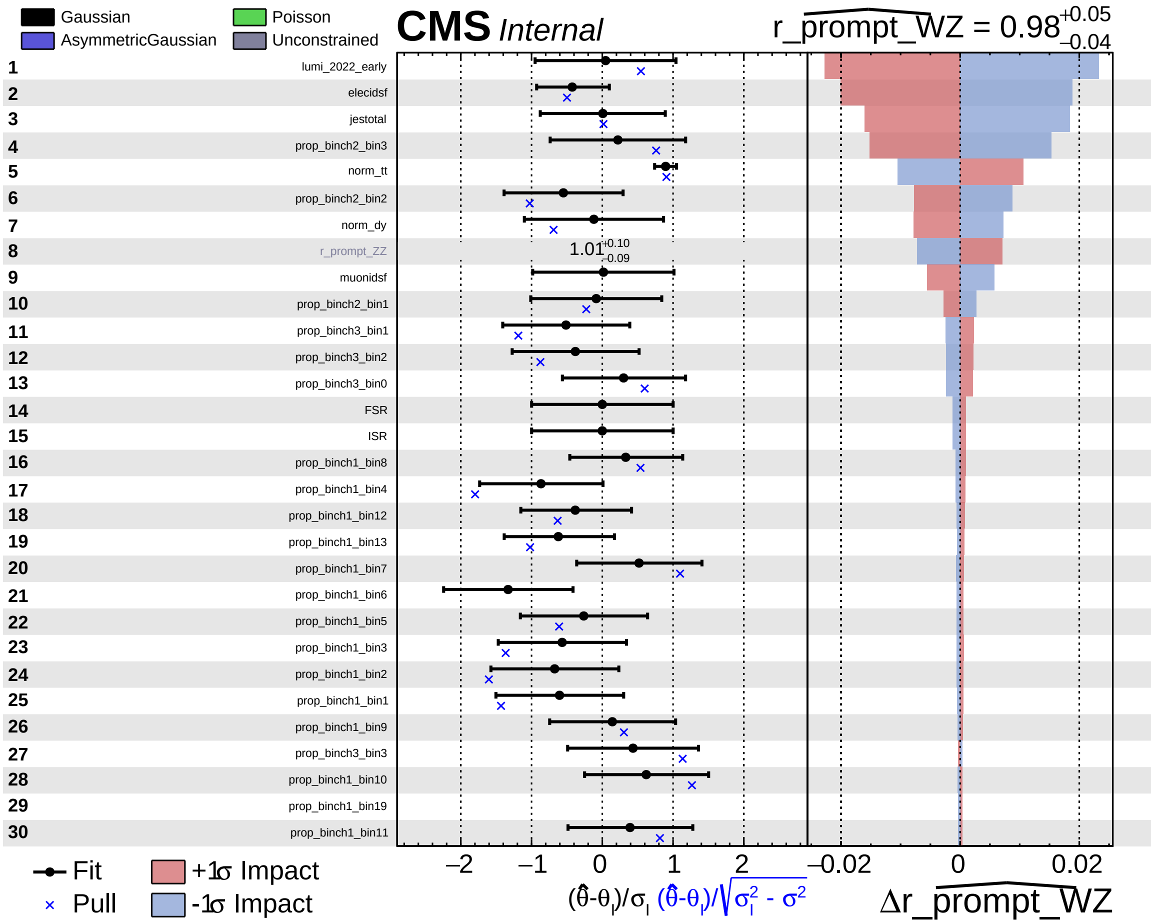

Figure 29: Impact of the different source of systematic uncertainty available for the Run 3 to the signal strength estimation of the WZ signal.

In Fig. 29, can be seen that the largest currently available contribution to the uncertainty is from the current luminosity and then, the one associated with the electrons efficiency. The fact that luminosity is now the one that most affects the value of this measure is interesting and can be associated with the fact that the rest of the uncertainties are constraining more with the real data than with the Asimov data.

We see that the third most significant contribution is that of the reconstruction of the jets. In addition we can see other important contributions such as the normalization of non-prompt backgrounds, where it can be seen in the uncertainty bars on the left how this has been constrained in *norm-tt* after being added to the fit. Also, looking at the left part of the figure, its is possible to see how the pre and post-fit are contributing and differing

Also, although in a already very small contribution, there are the muon efficiencies, ISR, FSR, the normalization of the ZZ background (which is practically null) and other statistical contributions.

With this, it has been possible to study a first measure of cross section for the WZ production process, where we have a signal strength of:

$$r_{wz-prompt} = \frac{\sigma_{exp}}{\sigma_{SM}} = 0.98^{+0.05}_{-0.04} \tag{38}$$

This first measurement of the production process WZ cross section at $\sqrt{s} = 13.6$ TeV has a result and uncertainties that are, initially, compatible with the value expected by the Standard Model theory.

Estimating identically to what was done without data, the logarithmic representation of the likelihood function is used to check the validity of our measure.

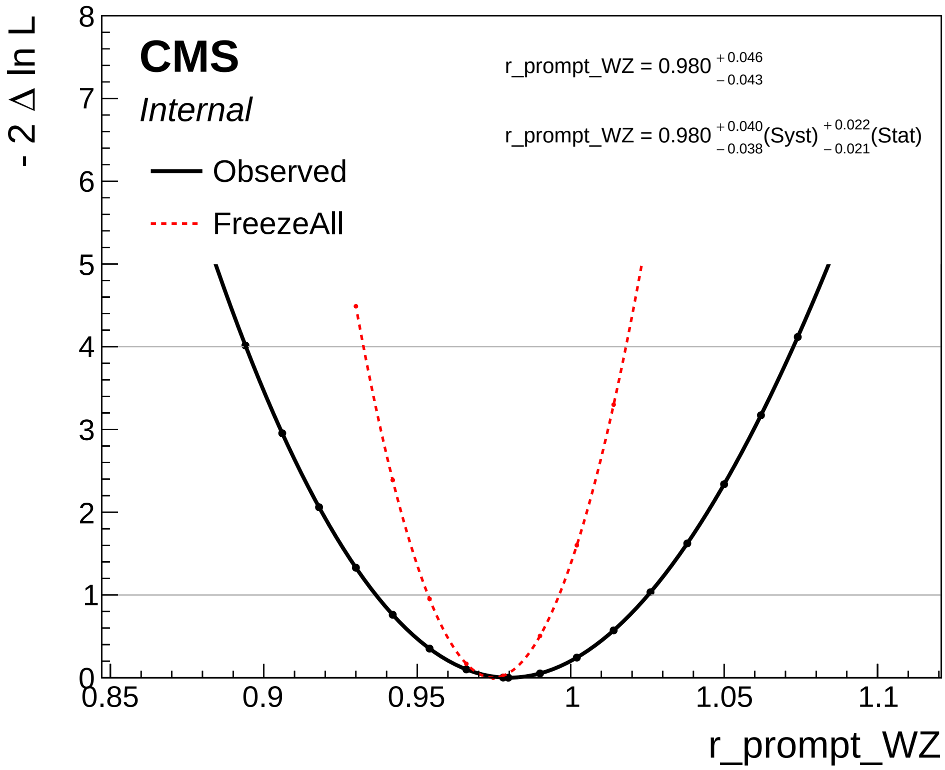

Figure 30: The fit ratio for the measurement of the expected WZ production cross section using the 2022 data from the CMS.

It is the study and estimation of all the uncertainties in association with the expected from the Standard Model cross section, where separating between systematic and statistical uncertainties:

$$r = 0.980 \ {}^{+0.040}_{-0.038} \ (Sys) \ {}^{+0.022}_{-0.021} \ (Stat) \tag{39}$$

Also, all this uncertainties are compatible compare with the ones obtained on the exhaustive and precise measurement done during the Run 2 in the WZ process, ([27]).

7 Conclusions

In this thesis, a detailed study of the WZ production process has been carried out. The measurement consisted of the extraction of the WZ signal from a likelihood fit to data by obtain simultaneously the normalization of WZ, ZZ and $t\bar{t}$, using the maximum likelihood fit to get a cross section of WZ. The signal extraction study using the control region of ZZ had already been done in previous WZ analyzes such as Run 2 ([27]) because it is the highest background in the WZ process. On the other hand, the measurement by adding the control region of the non-prompt top-antitop process for the fit, is the first time studied and has made it possible to reduce the uncertainty associated to this non-prompt background normalization.

It was obtained a signal strength of:

$$r \;=\; 0.980 \;\; ^{+0.040}_{-0.038} \; (Sys) \;\; ^{+0.022}_{-0.021} \; (Stat) \tag{40}$$

which is perfectly in agreement with what is expected from the Standard Model theory and according to what is expected by previous studies and the uncertainties are perfectly compatible:

Energy	Luminosity (fb^{-1})	Signal strenght values
$\sqrt{s} = 7$ TeV	4.9	1.05 $\pm$ 0.07 (stat.) $\pm$ 0.06(sys)
$\sqrt{s} = 8$ TeV	19.6	1.02 $\pm$ 0.04 (stat) $\pm$ 0.07 (sys)
$\sqrt{s} = 13$ TeV	137	1.00 $\pm$ 0.02 (stat) $\pm$ 0.03 (sys)
$\sqrt{s} = 13.6$ TeV	29.6	0.98 $\pm$0.02 (Stat) $\pm$0.04 (Sys)

Table 7: Representation of all the measurement of the WZ cross section at different center-of-mass energies by CMS ([17], [27]) adding the measure at $\sqrt{s} = 13.6$ TeV of this measurement. The uncertainties are included.

Run 3 has started in 2022, and will continue until the end of 2025. In this period it is expected to collect more than 250 fb^{-1} at 13.6 TeV. This amount of data will allow to improve the measurement presented here and to measure among others, the charge asymmetry in the production, the polarization of the W and Z bosons in WZ production, as well as differential distributions in both the inclusive and the charge-exclusive final states for several observables.

References

[1] Agostinelli, S., et al., *Geant4—a simulation toolkit*. Nuclear Instruments and Methods in Physics Research Section A: Accelerators, Spectrometers, Detectors and Associated Equipment. vol 506, n. 3, p. 250-303 (2003)

[2] Alioli, S. , Nason, P. , Oleari, C., and Re, E., *A general framework for implementing NLO calculations in shower Monte Carlo programs: the POWHEG BOX*. Journal of High Energy Physics, vol. 06, p. 043, 2010. DOI: 10.1007/JHEP062010043. arXiv: 1002.2581.

[3] Álvarez González, B., Cuevas, J., Erice, C. , Vischia, P., Folgueras, S. & Vico Villalba, C., *Status and future plans regarding WZ measurements during Run 3*. (2023).

[4] Alwall, J., Frederix, R., Frixione, S., Hirschi, V., Maltoni, F., Mattelaer, O., Shao, H.-S., Stelzer, T., Torrielli, P., and Zaro, M.. *The automated computation of tree-level and next-to-leading order differential cross sections, and their matching to parton shower simulations*. Journal of High Energy Physics, vol. 07, p. 079, 2014. arXiv: 1405.0301.

[5] ATLAS Collaboration, *Measurement of WZ production cross sections and gauge boson polarisation in p p collisions at $\sqrt{s} = 13$ TeV with the ATLAS detector*. Eur. Phys. J. C 79 (2019) 535. DOI: 10.1140/epjcs10052-019-7027-6. arXiv:1902.05759v2 (2019).

[6] ATLAS Collaboration, *Measurement of the ZZ production cross section in proton–proton collisions at $\sqrt{s} = 8$ TeV using the $ZZ \to l^- l^+ l'^- l'^+$ decay channels with the ATLAS detector*. J. High Energ. Phys. 01 (2017) 099. DOI: 10.1007/JHEP01(2017)099. arXiv:1610.07585v2.

[7] Bechtel, F. and Schleper, P., *The Underlying Event in Proton-Proton Collisions* (2023).

[8] Bertolini, D., Harris, P., Low, M. et al., *Pileup per particle identification.* J. High Energ. Phys. 2014, 59 (2014). https://doi.org/10.1007/JHEP10(2014)059

[9] Burgess, C. , & Moore, G. . The Standard Model: A Primer. Cambridge: Cambridge University Press. (2006). doi:10.1017/CBO9780511819698

[10] Cacciari M., Salam, G. P., and Soyez, G., *The anti-k_T jets clustering algorithm.* Journal of High Energy Physics, vol. 04, p. 063 (2008). DOI: 10.1088/1126-6708/2008/04/063.

[11] CMS Collaboration, *Observation of a new boson at a mass of 125 GeV with the CMS experiment at the LHC.* Physics Letters B. vol. 716, n.1,pag.30-61 (2012). doi = https://doi.org/10.1016/j.physletb.2012.08.021, arXiv: 1207.7235v2.

[12] CMS Collaboration. *Multi-year summary: proton-proton collisions at 13.6 TeV. Integrated and peak luminosity, 2021-2022 (Run 3).* https://cmslumi.web.cern.ch/publicplots/multiYear/int_lumi_allcumulative_pp_run3.pdf

[13] CMS Collaboration, *Particle-flow reconstruction and global event description with the CMS detector.* Journal Instrumentation, v.12, P10003, (2017). DOI: 10.1088/1748-0221/12/10/P10003. arXiv: 1706.04965

[14] CMS Collaboration, *Interactions per crossing (pileup) for 2022-2023, stacked plot.* https://cmslumi.web.cern.ch/publicplots/pileup_allYears_stack_run3.pdf

[15] CMS Collaboration, *Performance of t-lepton reconstruction and identification in CMS.* Journal of Instrumentation, vol. 7, P01001, 2012. doi: 10.1088/1748-0221/7/01/p01001.

[16] CMS Collaboration, *Measurement of electroweak WZ boson production and search for new physics in WZ + two electrones y muoness events in pp collisions at* $\sqrt{s} = 13$ *TeV*. Physics Letters B. v. 795. p.281 (2019).

[17] CMS Collaboration, *Measurement of the WZ production cross section in pp collisions at* $\sqrt{s}$ *= 7 and 8 TeV and search for anomalous triple gauge couplings at* $\sqrt{s}$ *=8 TeV*. European Physics Journal C, vol. 77, p. 236, 2017. doi: 10.1140/epjc/s10052-017-4730-z. arXiv: 1609.05721v2.

[18] CMS Collaboration, *Measurements of the electroweak diboson production cross sections in proton-proton collisions at* $\sqrt{s} =$ 5.02 *TeV using leptonic decays.* Phys. Rev. Lett. 127, 191801. DOI:https://doi.org/10.1103/PhysRevLett.127.191801 (2021).

[19] CMS Collaboration, *Di-boson cross section ratio comparison to theory.* https://twiki.cern.ch/twiki/bin/view/CMSPublic/PhysicsResultsCombined.

[20] CMS Collaboration, *The CMS Tracker system project: Technical Design Report* (1997).

[21] CMS Collaboration, *The CMS electromagnetic calorimeter project: Technical Design Report* (1997).

[22] CMS Collaboration, *The CMS hadronic calorimeter project: Technical Design Report* (1997).

[23] CMS Collaboration, *The CMS muon project: Technical Design Report* (1997.)

[24] CMS Collaboration, *Identification of heavy-flavour jets with the CMS detector in pp collisions at 13 TeV*. Journal of Instrumentation, vol. 13, P05011, 2018. doi: 10.1088/1748-0221/13/05/P05011. arXiv: 1712.07158.

[25] CMS Collaboration, *Performance of electron and photon reconstruction in Run 2 with the CMS experiment*, Detectors and Experimental Techniques Report: CMS-DP-2020-037; CERN-CMS-DP-2020-037.

[26] CMS Collaboration, *Muon reconstruction performance during Run II.* Detectors and Experimental Techniques Report: CMS-DP-2019-022; CERN-CMS-DP-2019-022.

[27] CMS Collaboration., Tumasyan, A., Adam, W. et al., *Measurement of the inclusive and differential WZ production cross sections, polarization angles, and triple gauge couplings in pp collisions at* $\sqrt{s} = 13TeV$, J. High Energ. Phys. 2022, 32 (2022). https://doi.org/10.1007/JHEP07(2022)032.

[28] Defranchis, M. M., *Event Reconstruction in CMS. In: First Measurement of the Running of the Top Quark Mass.* Springer Theses. Springer, Cham. DOI: /10.1007/978-3-030-90376-3_4

[29] Di Lella, L. and Rubbia, C., *The Discovery of the W and Z Particles.* Adv. Ser. Direct. High Energy Phys., v. 23, p. 137-163. doi = 10.1142/9789814644150_0006. (2015)

[30] Donoghue, J. F. , Golowich E. , Holstein B.R., *Dynamics of the Standard Model.* Second Edition, Cambridge University Press (2014).

[31] Englert, F. & Brout, R. *Broken symmetry and the mass of gauge vector mesons.* Physical Review Letters, vol. 13, p. 321 (1964). DOI: 10.1103/PhysRevLett.13.321.

[32] Erice, C., *Study of beyond the Standard Model processes in leptonic final states with the CMS detector at the Run II of the LHC.* PhD, University of Oviedo (2021). https://cds.cern.ch/record/2783303.

[33] ERLER, J. , FREITAS, A., ET AL. *Review of the Standard Model.* Particle Data Group (2019)

[34] ESMA MOBS. *The CERN accelerator complex-August 2018. Complexe des accélérateurs du CERN-Août 2018.* August 2018. General Photo.

[35] FOCARDI, E. , *Status of the CMS Detector.* Physical Procedia v.37 (2012). 10.1016/j.phpro.2012.02.363

[36] GARLING, D. J. H., *Clifford algebras. An introduction*, London Mathematical Society Student Texts, vol. 78, Cambridge University Press (2011). ISBN 978-1-107-09638-7.

[37] HERR, W. & MURATORI, B. *Concept of Luminosity* CERN (2006).

[38] HIGGS, P. W. *Spontaneous symmetry breakdown without massless bosons.* Physical Review Letter, vol 145, p. 1156 (1966). DOI: 10.1103/PhysREv.145.1156

[39] MARTIN, A.D., STIRLING, W.J., THORNE, R.S., WATT, G., *Parton distributions for the LHC.*The European Physical Journal C, 63(2):189–285 (2009). arXiv:0901.0002

[40] PARTICLE DATA GROUP, ET AL., *Progress of Theoretical and Experimental Physics*, Volume 2022, Issue 8, August 2022, 083C01, https://doi.org/10.1093/ptep/ptac097

[41] RODRÍGUEZ BOUZA, V., *Measurement of inclusive and differential cross sections for single top quark production in association with a W boson in proton-proton collisions at* $\sqrt{s} = 13$ *TeV*. PhD, University of Oviedo (2023). https://cds.cern.ch/record/2856746.

[42] Schwartz, M., *Quantum Field Theory and the Standard Model.* Cambridge: Cambridge University Press. doi:10.1017/9781139540940 (2013).

[43] Sirunyan, A.M. et al. *Performance of the CMS muon detector and muon reconstruction with proton-proton collisions at* $\sqrt{s} = 13\,TeV$. (2018) DOI: 10.1088/1748-0221/13/06/P06015. arXiv:1804.04528CMS-MUO-16-001CERN-EP-2018-058

[44] Sjöstrand, T., Mrenna, S., & Skands, P.. *A brief introduction to pythia 8.1.* Computer Physics Communications, 178(11):852–867, Jun 2008.

[45] Tomé, C., *Del Modelo Estándar.* Cultura Científica (2014). https://culturacientifica.com/2014/06/17/del-modelo-estandar/

[46] Tournefier, E., *The preshower detector of CMS at LHC.* Nuclear Instruments and Methods in Physics Research Section A: Accelerators, Spectrometers, Detectors and Associated Equipment. v. 461, p355-360, (2001). DOI: 10.1016/0168-9002(00)01243-2.

[47] Wess, J. & Bagger, J.*Supersymmetry and supergravity.* Princeton University Press, (1992). ISBN = "978-0-691-02530-8.

Appendix

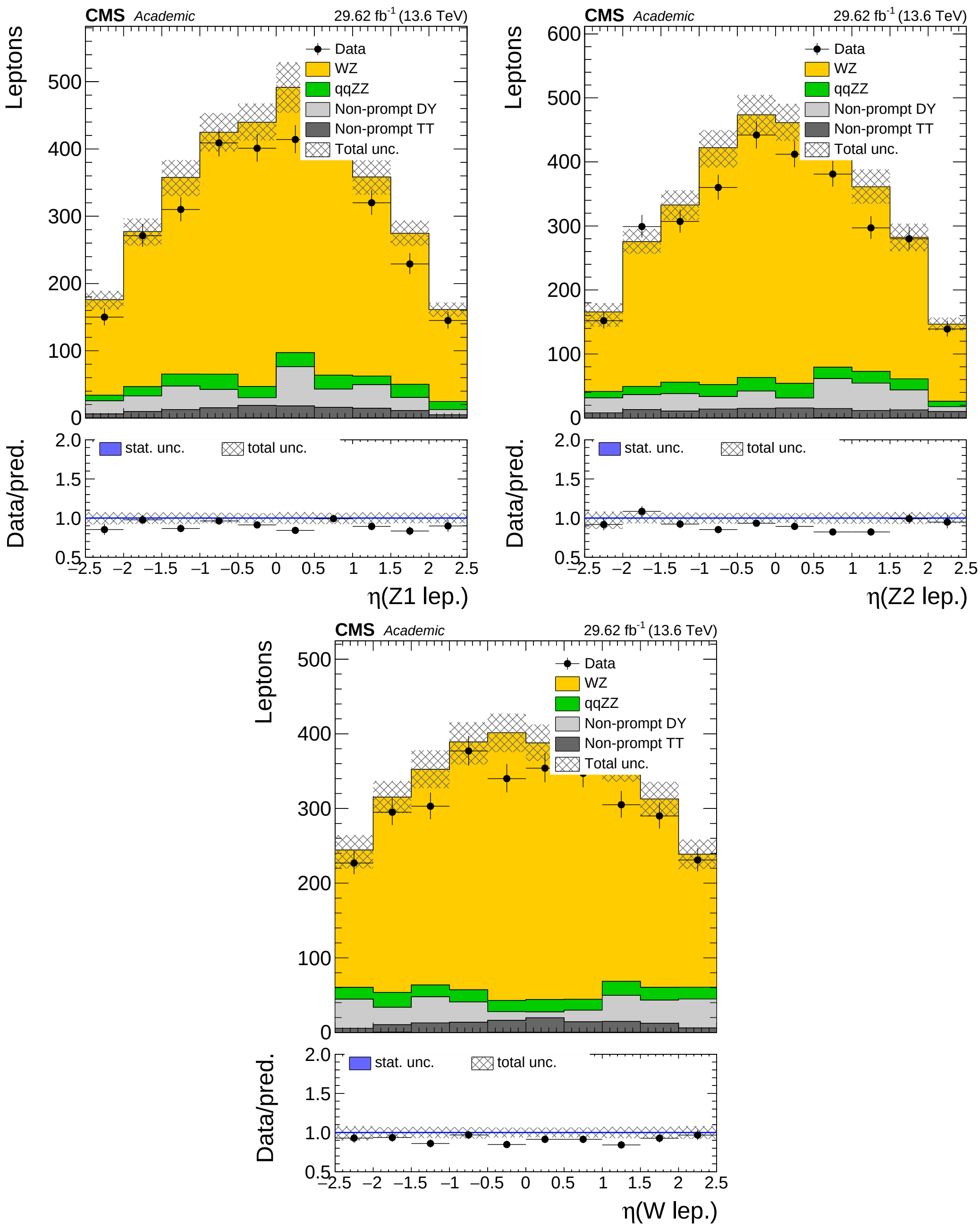

Figure 31: Representation of the pseudorapities distributions of the two leptons from Z and the lepton from W in the signal region of WZ.

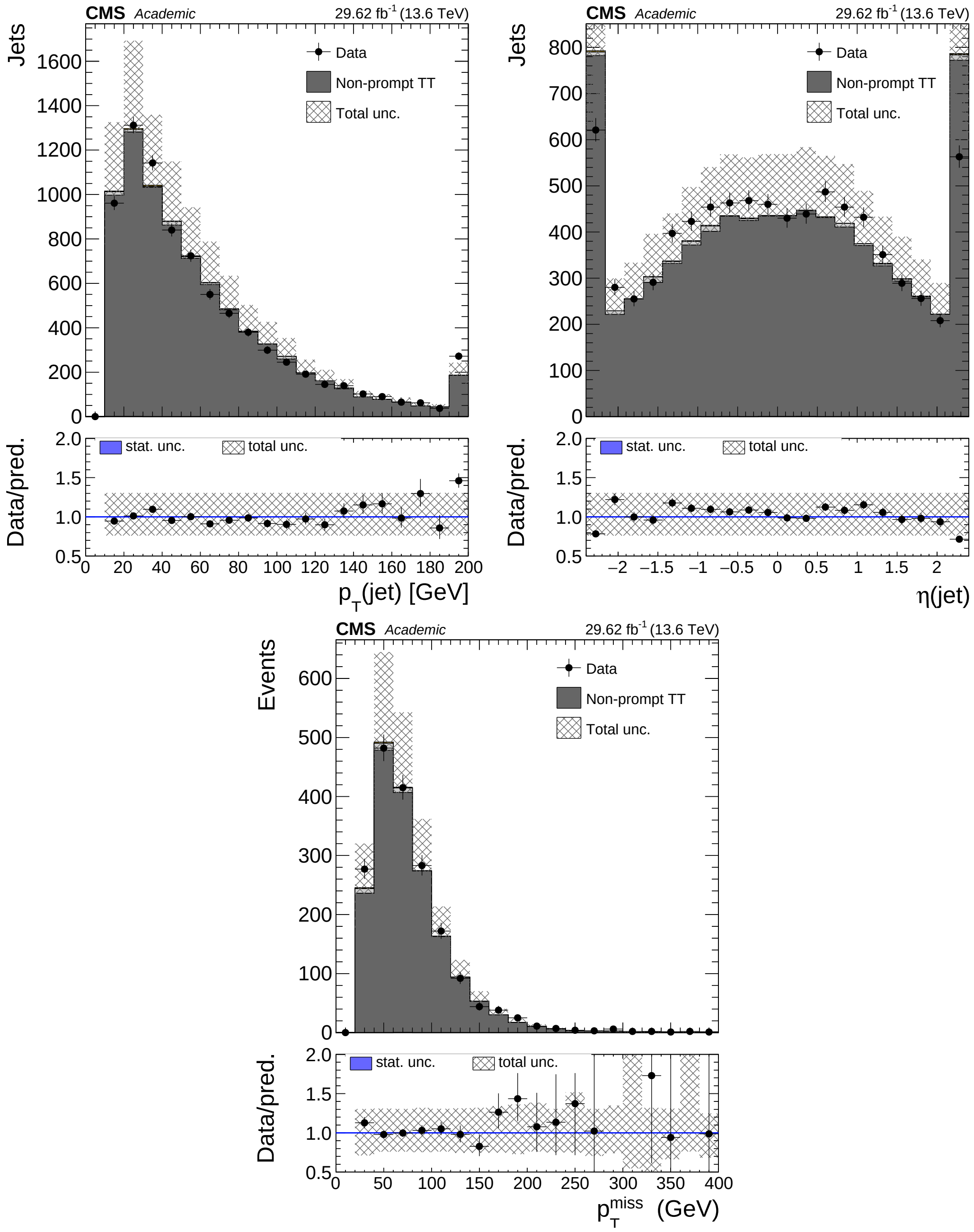

Figure 32: Representation of distribution of events of the momentum and pseudorapidity of the more energetic jet and the missing transverse energy in the $t\bar{t}$ control region.

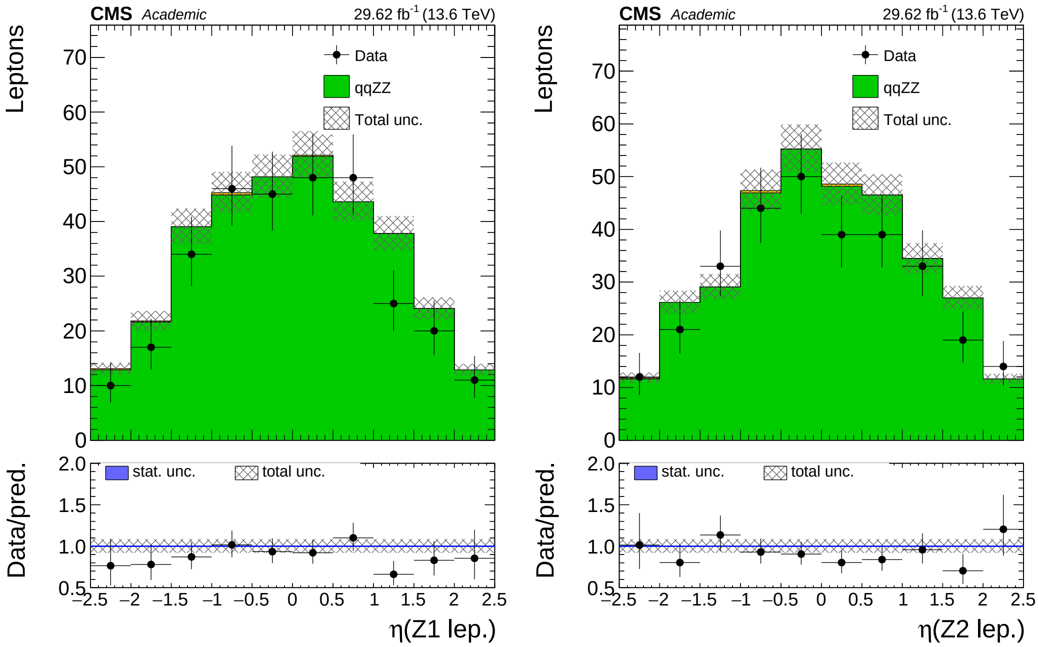

Figure 33: Representation of the pseudorapities distributions of the two leptons coming from the Z boson in the control region of ZZ.